

# Molecular Gas in NUClei of GALaxies (NUGA): IX. The decoupled bars and gas inflow in NGC 2782 <sup>\*</sup>

L.K. Hunt<sup>1</sup>, F. Combes<sup>2</sup>, S. García-Burillo<sup>3</sup>, E. Schinnerer<sup>4</sup>, M. Krips<sup>5</sup>, A.J. Baker<sup>6</sup>, F. Boone<sup>2</sup>, A. Eckart<sup>7</sup>, S. León<sup>8</sup>, R. Neri<sup>9</sup>, and L.J. Tacconi<sup>10</sup>

<sup>1</sup> INAF-Istituto di Radioastronomia/Sez. Firenze, Largo Enrico Fermi 5, 50125 Firenze, Italy; e-mail: [hunt@arcetri.astro.it](mailto:hunt@arcetri.astro.it)

<sup>2</sup> Observatoire de Paris, LERMA, 61 Av. de l'Observatoire, F-75014, Paris, France

<sup>3</sup> Observatorio Astronómico Nacional (OAN) - Observatorio de Madrid, C/ Alfonso XII, 3, 28014 Madrid, Spain

<sup>4</sup> Max-Planck-Institut für Astronomie, Königstuhl 17, D-69117 Heidelberg, Germany

<sup>5</sup> Harvard-Smithsonian Center for Astrophysics, SMA, 645 N. A'ohoku Pl., Hilo, HI 96720 USA

<sup>6</sup> Department of Physics and Astronomy, Rutgers, State University of New Jersey, 136 Frelinghuysen Road, Piscataway, NJ 08854, USA

<sup>7</sup> I. Physikalisches Institut, Universität zu Köln, Zùlpicherstrasse 77, 50937-Köln, Germany

<sup>8</sup> IRAM-Pico Veleta Observatory, Avenida Divina Pastora 7, Local 20 E-18012 Granada, Spain

<sup>9</sup> IRAM-Institut de Radio Astronomie Millimétrique, 300 Rue de la Piscine, 38406-St.Mt.d'Hères, France

<sup>10</sup> Max-Planck-Institut für extraterrestrische Physik, Postfach 1312, D-85741 Garching, Germany

Received ; accepted

**Abstract.** We present CO(1-0) and CO(2-1) maps of the starburst/Seyfert 1 galaxy NGC 2782 obtained with the IRAM interferometer, at  $2''.1 \times 1''.5$  and  $0''.7 \times 0''.6$  resolution respectively. The CO emission is aligned along the stellar nuclear bar of radius  $\sim 1$  kpc, configured in an elongated structure with two spiral arms at high pitch angle  $\sim 90^\circ$ . At the extremity of the nuclear bar, the CO changes direction to trace two more extended spiral features at a lower pitch angle. These are the beginning of two straight dust lanes, which are aligned parallel to an oval distortion, reminiscent of a primary bar, almost perpendicular to the nuclear one. The two embedded bars appear in Spitzer IRAC near-infrared images, and HST color images, although highly obscured by dust in the latter. We compute the torques exerted by the stellar bars on the gas, and find systematically negative average torques down to the resolution limit of the images, providing evidence of gas inflow tantalizingly close to the nucleus of NGC 2782. We propose a dynamical scenario based on numerical simulations to interpret coherently the radio, optical, and molecular gas features in the center of the galaxy. Star formation is occurring in a partial ring at  $\sim 1.3$  kpc radius corresponding to the Inner Lindblad Resonance (ILR) of the primary bar; this ring-like structure encircles the nuclear bar, and is studded with H $\alpha$  emission. The gas traced by CO emission is driven inward by the gravity torques of the decoupled nuclear bar, since most of it is inside its corotation. N-body simulations, including gas dissipation, predict the secondary bar decoupling, the formation of the elongated ring at the  $\sim 1$  kpc-radius ILR of the primary bar, and the gas inflow to the ILR of the nuclear bar at a radius of  $\sim 200$ -300 pc. The presence of molecular gas inside the ILR of the primary bar, transported by a second nuclear bar, is a potential “smoking gun”; the gas there is certainly fueling the central starburst, and in a second step could fuel directly the AGN.

**Key words.** Galaxies: individual (NGC 2782) – Galaxies: starburst – Galaxies: spiral – Galaxies: kinematics and dynamics — Galaxies: interstellar matter

## 1. Introduction

Molecular gas is the dominant gas component in the inner regions of spiral galaxies, making CO lines unique tracers of nuclear gas dynamics. As such, they are also a powerful diagnostic for identifying how active nuclei (AGN) are fueled. To feed an AGN through accretion, there must

Send offprint requests to: [hunt@arcetri.astro.it](mailto:hunt@arcetri.astro.it)

<sup>\*</sup> Based on observations carried out with the IRAM Plateau de Bure Interferometer. IRAM is supported by the INSU/CNRS (France), MPG (Germany), and IGN (Spain).

be an adequate supply of gas whose angular momentum has been sufficiently reduced to enable inflow within the small spatial scales surrounding the black hole. Although there is rarely a lack of circumnuclear fuel, it is not yet clear how angular momentum is removed to enable nuclear accretion.

To better understand how AGN are fed and maintained, we have been conducting for several years now a high-resolution high-sensitivity CO survey (NUGA, García-Burillo et al. 2003) of galaxies at the IRAM Plateau de Bure Interferometer (PdBI). Altogether we have observed 12 galaxies in two CO transitions with up to four configurations of the array, so as to achieve the most sensitive (typically  $\sim 2 - 4$  mJy beam $^{-1}$  in 10 km s $^{-1}$  channels) and the highest resolution (1-2'') survey currently available. The results of the NUGA survey so far have been surprising: there is no single unambiguous circumnuclear molecular gas feature connected with the nuclear activity. One- and two-armed instabilities (García-Burillo et al. 2003), well-ordered rings and nuclear spirals (Combes et al. 2004), circumnuclear asymmetries (Krips et al. 2005), and large-scale bars (Boone et al. 2007) are among the variety of molecular gas morphologies revealed by our survey. Moreover, an analysis of the torques exerted by the stellar gravitational potential on the molecular gas in four galaxies suggests that the gas tends to be driven away from the the AGN ( $\gtrsim 50$  pc), rather than toward it (García-Burillo et al. 2005). Nevertheless, these dynamics do not correspond to the violent molecular outflows and superwinds predicted in AGN feedback models (e.g., Narayanan et al. 2006; Hopkins & Hernquist 2006), because the observed velocities are much too small.

Much of the explanation of this variety of morphologies appears to be related to timescales (García-Burillo et al. 2005). It is well established that large-scale bars transport gas inward very efficiently (e.g., Combes & Gerin 1985; Sakamoto et al. 1999), and there is very little doubt that bars can drive powerful starbursts (Knapen et al. 2002; Jogee et al. 2005). However, no clear correlation between bars and nuclear activity has yet been found (e.g., Mulchaey & Regan 1997). This may be because the timescales for bar-induced gas inflow and AGN duty cycles are very different. Bars drive inflow over timescales ( $\gtrsim 300$  Myr) that are similar to the typical gas-consumption timescales of a few times  $\sim 10^8$  yr found in nuclear starbursts (e.g., Jogee et al. 2005). But AGN accretion-rate duty cycles are much shorter than this ( $\sim 1$ -10 Myr, Heckman et al. 2004; Hopkins & Hernquist 2006; King & Pringle 2007), and there are several indications that active accretion occurs only intermittently over the lifetime of a galaxy (Ferrarese et al. 2001; Marecki et al. 2003; Janiuk et al. 2004; Hopkins & Hernquist 2006; King & Pringle 2007). The resulting implication is that most AGN are probably between active accretion episodes,

and catching galaxies with nuclear accretion “switched on” may be difficult.

In this paper, the ninth of the NUGA series, we present observations that suggest that we have found one of these potentially rare AGN with possible gas inflow in the current epoch. NGC 2782 is an early-type spiral galaxy [SABa(rs)] with peculiar morphology. In addition to a pronounced stellar tail or sheet  $\sim 20$  kpc to the east, it shows three optical ripples (e.g., Smith 1994) thought to be signatures of tidal interactions (Schweizer & Seitzer 1988). A massive HI plume extends  $\sim 54$  kpc to the northwest, and the neutral atomic gas in the inner disk is counterrotating with respect to the gas motions in the outer regions (Smith 1991). The central regions of NGC 2782 host a massive nuclear starburst, with a far-infrared (FIR) luminosity of  $2 \times 10^{10} M_{\odot}$ , comparable to that in M 82 (Devereux 1989). Three-dimensional optical spectroscopy (Yoshida et al. 1999) shows evidence for a high-speed ionized gas outflow, with the bipolar structure in the radio continuum indicative of a confined superbubble (Jogee et al. 1998). In the outflow, there are also high-excitation extranuclear emission lines thought to be due to shock heating (Boer et al. 1992).

Until recently, it was thought that the outflow and energetics in NGC 2782 were powered by a starburst alone, but recent radio and X-ray observations reveal an optically-hidden AGN. MERLIN and EVN/VLBI observations show a high-brightness-temperature extremely compact ( $\lesssim 0''.05$ ) radio source, unambiguous evidence of an AGN (Krips et al. 2007). NGC 2782 is also a Compton-thick X-ray source with a 6.4 keV iron feature coming from its innermost regions (Zhang et al. 2006). There is a bright unresolved X-ray core and extended emission roughly coincident with the radio morphology in the high-resolution ( $\sim 1''$ ) image by Saikia et al. (1994).

The nuclear region of NGC 2782 has been observed previously in the  $^{12}\text{CO}(1-0)$  line by Ishuzuki (1994) with the Nobeyama Millimeter Array and by Jogee et al. (1999) using the Owens Valley Radio Observatory. We reobserved NGC 2782 in  $^{12}\text{CO}(1-0)$  at PdBI with better spatial resolution and a sensitivity roughly five times that of previous observations, and for the first time in the  $^{12}\text{CO}(2-1)$  line. This enables a rigorous derivation of the torques acting on the molecular gas in NGC 2782, and a quantitative assessment of the infall of material to the nucleus. We first present our new observations in Section 2, together with our multiwavelength imaging dataset. The morphology and kinematics of the molecular gas are discussed in Section 3, and we describe the stellar structure in Section 4 and the starburst episode in Section 5. We then derive the gravitational potential from the infrared image, and infer the torques acting on the molecular gas in Section 6. Finally, we present numerical simulations which motivate our proposed scenario of decoupled double bars in this galaxy. The molecular gas in NGC 2782 is apparently being driven inward by the nuclear bar, decoupled from the

primary bar, since we detect azimuthally averaged torques which are negative down to the resolution limit of our images.

## 2. Observations

We observed NGC 2782 with the IRAM PdBI in the ABCD configuration of the array between December 2001 and February 2003 in the  $^{12}\text{CO}(1-0)$  (115 GHz) and the  $^{12}\text{CO}(2-1)$  (230 GHz) rotational transitions. The PdBI receiver characteristics, the observing procedures, and the image reconstruction are the same as those described in García-Burillo et al. (2003). The quasar 3C273 was used for bandpass calibration and the quasar 0923+392 was used to calibrate both the phase and the atmospheric variations. We used uniform weighting to generate 2–1 maps with a field of view of  $21''$  and natural weighting to produce the 1–0 maps with a field of view of  $42''$ . Such a procedure maximizes the flux recovered in CO(1–0) and optimizes the spatial resolution in CO(2–1).

The *rms* noise  $\sigma$  in  $10\text{ km s}^{-1}$  wide velocity channels is  $2.0\text{ mJy beam}^{-1}$  and  $5.2\text{ mJy beam}^{-1}$ , with beam sizes of  $2''.1 \times 1''.5$  and  $0''.7 \times 0''.6$  at 115 and 230 GHz, respectively. At a level of  $\sim 3\sigma$ , no 3 mm (1 mm) continuum is detected toward NGC 2782 to a level of  $1\text{ mJy beam}^{-1}$  ( $3\text{ mJy beam}^{-1}$ ). The conversion factors between  $\text{Jy beam}^{-1}$  and K are  $30\text{ K Jy}^{-1}\text{ beam}$  at 115 GHz, and  $58\text{ K Jy}^{-1}\text{ beam}$  at 230 GHz. By default, all velocities are referred to the heliocentric recession velocity  $v_0 = 2545\text{ km s}^{-1}$  and  $(\Delta\alpha, \Delta\delta)$  offsets are relative to the phase tracking center of the observations (RA<sub>2000</sub>, Dec<sub>2000</sub>) =  $(09^{\text{h}}14^{\text{m}}05.08^{\text{s}}, 40^{\text{d}}06^{\text{m}}49.4^{\text{s}})$ . The displayed maps are not corrected for primary beam attenuation.

We will assume a distance to NGC 2782 of  $D = 35\text{ Mpc}$ , which is derived from the local velocity field model given in Mould et al. (2000) and a Hubble constant  $H_0 = 73\text{ km s}^{-1}\text{ Mpc}^{-1}$ . At this distance  $1''$  corresponds to  $171\text{ pc}$ .

### 2.1. Optical and infrared images

We retrieved *HST* archival images of NGC 2782 with WFPC2 in the F555W and F814W filters. Cosmic rays were eliminated, and the images were calibrated and converted to *V* and *I* as described in Holtzman et al. (1995). We performed an astrometric calibration using stars from the U.S. Naval Observatory Astrometric Catalog B1.0 (USNO-B1.0). Five stars from this catalogue appear in the  $1600 \times 1600$  WFPC2 image of NGC 2782 and they were used to derive the astrometric solution with *imwcs* in the WCSTools package<sup>1</sup>. The solution has an rms uncertainty of  $0''.24$ , or 2.4 WFPC2 (mosaic) pixels, and differs from the original *HST* one by  $\gtrsim 1''$ . We made *V*–*I* color images

by converting the flux units to magnitudes and subtracting the two magnitude images.

IRAC images at  $3.6\ \mu\text{m}$  were retrieved from the *Spitzer* archive. We started with the Basic Calibrated Data images, and aligned and combined them with MOPEX (Makovoz & Marleau 2005) which accounts for distortion and rotates to a fiducial coordinate system.  $1''.20$  pixels were imposed for the final image, roughly the same as the original IRAC detector. Significant banding was present from a bright star in the field, and this was corrected for by interpolation over the affected rows before combination with MOPEX. Combination of these corrected images showed no discernible effect of the original flaw.

The infrared and optical images will be discussed in Sections 4 and 5.

## 3. Molecular gas results

Figures 1 and 2 show the velocity-channel maps of  $^{12}\text{CO}(1-0)$  and  $^{12}\text{CO}(2-1)$  emission in the central region of NGC 2782. The kinematics show the typical signature of a rotating disk, together with non-circular motions more prominent to the south. The western (eastern) side of the CO bar is red- (blue-) shifted relative to the systemic velocity  $V_{\text{sys}}$ , which is fitted to be at  $2555 \pm 10\text{ km s}^{-1}$ . This agrees very well with the H I heliocentric velocity of  $2555\text{ km s}^{-1}$  (Smith 1994).

The dynamical center was derived from the center of symmetry of the velocity field, and chosen to maximize the velocity dispersion. It is determined to lie at  $(\alpha_{2000}, \delta_{2000}) = (09^{\text{h}}14^{\text{m}}05.11^{\text{s}}, 40^{\circ}06'49.24'')$ , not far from the phase-tracking center. The position of the dynamical center coincides almost exactly with the compact radio source discovered by Krips et al. (2007):  $(\alpha_{2000}, \delta_{2000}) = (09^{\text{h}}14^{\text{m}}05.11^{\text{s}}, 40^{\circ}06'49.32'')$ . Both are also within the errors of the position of the “C” component of the NGC 2782 nucleus described by Saikia et al. (1994). Therefore we ascribe the position of the AGN and the dynamical center of NGC 2782 to the position derived here from the CO kinematics.

### 3.1. CO morphology

The overall distribution of the molecular gas is illustrated in Figure 3 which shows the velocity-integrated CO intensity maps, achieved by integrating channels from  $v = -230$  to  $230\text{ km s}^{-1}$ . The naturally weighted  $^{12}\text{CO}(1-0)$  map is shown in the top panel of Fig. 3, and the uniform-weight  $^{12}\text{CO}(2-1)$  map in the bottom panel. After correcting for primary beam attenuation and considering only measurements with a signal-to-noise of  $3\sigma$  or greater on the data cube, our naturally weighted (1–0) observations in the central  $42''$  detect an integrated CO flux of  $150\text{ Jy km s}^{-1}$ . This corresponds to 65% of that in the Five College Radio Astronomy Observatory single dish mea-

<sup>1</sup> Available from <http://tdc-www.harvard.edu/software/wcstools>

measurements (within  $45''$ :  $230 \text{ Jy km s}^{-1}$ , Young et al. 1995), and roughly 78% of the flux measured by Jogee et al. (1999,  $195 \text{ Jy km s}^{-1}$ ). Our measurements are sensitive to small-scale structure but are missing some fraction of the diffuse component. We use the short-spacing single dish observations by Young et al. (1995) to derive the gas mass for numerical simulations in Sect. 7.3.

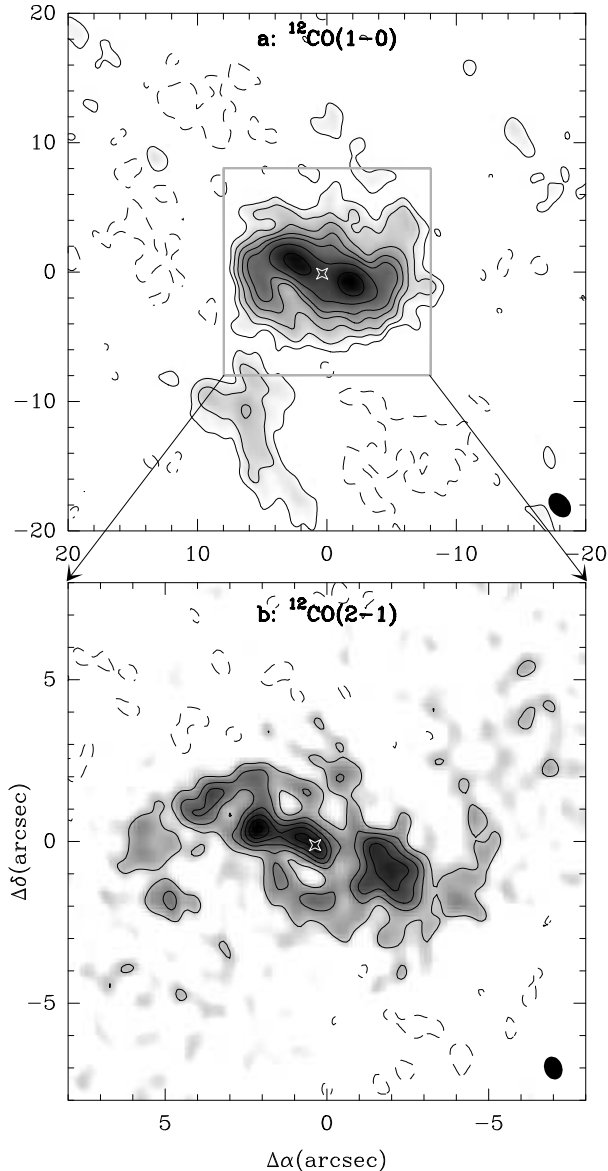


**Fig. 3.** Top panel: **a)** The natural-weight map in  $^{12}\text{CO}(1-0)$  (top panel) and  $^{12}\text{CO}(2-1)$  (bottom). The star marks the position of the AGN (coincident with the dynamical center). The kinematic signature of a rotating disk is clearly seen in Fig. 4, and in the body of the circumnuclear molecular spiral, there are few non-circular motions. However, the southern spiral arm in the  $^{12}\text{CO}(1-0)$  map (top panel of Fig. 4) shows clear streaming motions, and appears to be somewhat decoupled from the nuclear spiral because of the velocity discontinuity toward the southeast. In the bottom panel of Fig. 4, systematic kinks appear in the  $^{12}\text{CO}(2-1)$

The  $^{12}\text{CO}(1-0)$  emission is distributed in a nuclear elongated structure already identified by Jogee et al.

(1999). Our observations clearly delineate the diffuse spiral arms extending to the north and south. The spirals are not symmetric, and there is substantially more emission to the southeast than to the northwest. The filaments at  $\sim 10''$  to the north and south in  $^{12}\text{CO}(1-0)$  correspond to the spiral arms from the outer stellar oval (which we discuss in more detail below). Indeed, the CO “spur” labeled “O2” by Jogee et al. (1999) appears to be associated with the extended southern spiral arm shown in our maps (see Fig. 3).

The central structure in the  $^{12}\text{CO}(2-1)$  map is clearly resolved; the higher resolution afforded by our new observations shows a clearly elongated structure with spiral arms commencing at the ends of the elongation. The gas in the inner spiral arms is aligned along the elongation with a pitch angle of  $\sim 90^\circ$ , which makes the feature resemble more a bar than an inclined or edge-on disk. At the end of the feature, the gas changes direction to follow the outer spiral arms, which are situated at a lower pitch angle. Moreover, the molecular gas is clearly responding to the stellar oval/bar which we will discuss in Section 4. Hence, we will refer to the circumnuclear molecular structure as the “nuclear gas bar”, as distinct from the nuclear stellar bar (see below).

The molecular gas mass within the  $42''$  PdB primary beam field is  $M_{\text{H}_2} = 1.4 \times 10^9 M_\odot$ , assuming the CO-to- $\text{H}_2$  conversion factor  $X = 2.2 \times 10^{20} \text{ cm}^{-2} (\text{K km s}^{-1})^{-1}$  given by Solomon & Barrett (1991). Including the helium mass in the clouds (multiplying  $\times 1.36$ ) gives  $M_{\text{H}_2 + \text{He}} = 1.9 \times 10^9 M_\odot$ . Most of the molecular gas mass in NGC 2782 is in the nuclear gas bar+spiral, making it an extremely massive structure. Indeed, the circumnuclear molecular gas component in NGC 2782 is particularly massive, roughly 3 times more so than most of the NUGA galaxies studied so far (NGC 4826: García-Burillo et al. 2003, NGC 7217: Combes et al. 2004, NGC 3718: Krips et al. 2005, NGC 4579: García-Burillo et al. 2005, NGC 6951: García-Burillo et al. 2005 all have molecular masses on the order of  $\sim 3 \times 10^8 M_\odot$ ). Only NGC 4569 (Boone et al. 2007), with  $M_{\text{H}_2} = 1.1 \times 10^9 M_\odot$ , is roughly comparable with NGC 2782.

### 3.2. Kinematics

Figure 4 shows the mean velocity field derived from  $^{12}\text{CO}(1-0)$  and  $^{12}\text{CO}(2-1)$ . The kinematic signature of a rotating disk is clearly seen in Fig. 4, and in the body of the circumnuclear molecular spiral, there are few non-circular motions. However, the southern spiral arm in the  $^{12}\text{CO}(1-0)$  map (top panel of Fig. 4) shows clear streaming motions, and appears to be somewhat decoupled from the nuclear spiral because of the velocity discontinuity toward the southeast. In the bottom panel of Fig. 4, systematic kinks appear in the  $^{12}\text{CO}(2-1)$

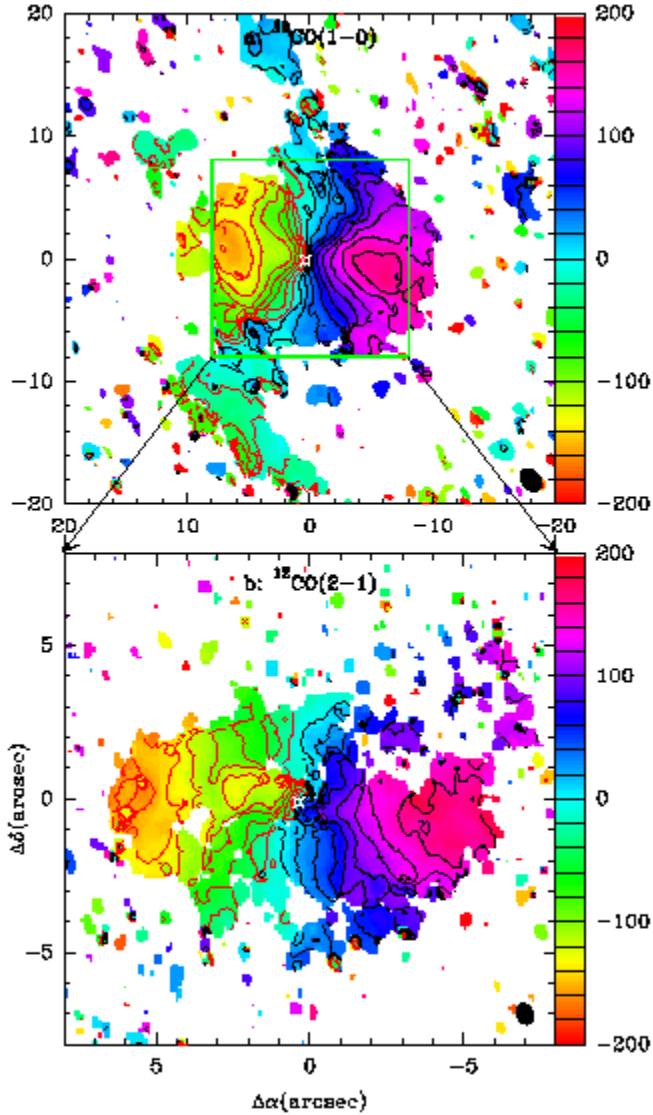


**Fig. 4.**  $^{12}\text{CO}(1-0)$  (a: top panel) and  $^{12}\text{CO}(2-1)$  (b: bottom) isovelicities contoured over false-color velocity maps. The AGN (dynamical center) position is marked with a star.

We derive a kinematic major axis of  $\text{PA} = (75 \pm 5)^\circ$ , consistent with previous determinations ( $75^\circ$ , Jogee et al. 1999). We will assume that the inclination angle of the nuclear spiral in NGC 2782 is  $\sim 30^\circ$  (see also Jogee et al. 1999). A smaller inclination would result in  $\sin i$  corrected velocities which would be too large to be consistent with even the largest spiral galaxies and ellipticals. A larger inclination seems equally unlikely because of the relatively straight extended spiral arms (see discussion in Sect. 5); if

the inclination were  $\gtrsim 30^\circ$ , the arms would be apparently more compressed relative to the line of nodes. That the galaxy disk is inclined at  $30^\circ$  is confirmed by the two-dimensional bulge-disk decomposition and the elliptical isophote fitting described in Sect. 4.

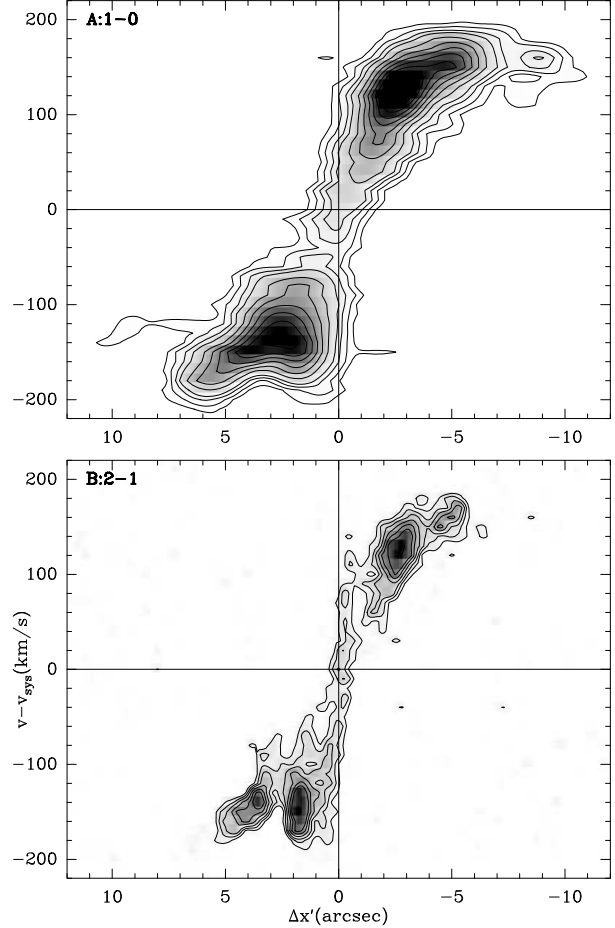


**Fig. 5.** Top panel: a) Position-velocity diagram of  $^{12}\text{CO}(1-0)$  along the kinematic major axis of NGC 2782 ( $\text{PA} = 75^\circ$ ) contoured over a grey-scale representation. Velocities have been rescaled to  $V_{\text{sys}} = 2555 \text{ km s}^{-1}$ , and offsets are relative to the dynamical center. Bottom panel: b) The same for  $^{12}\text{CO}(2-1)$ .

Position-velocity (PV) diagrams along the major kinematic axis of NGC 2782 are shown in Fig. 5, and along the minor axis in Fig. 6. In both figures,  $^{12}\text{CO}(1-0)$  is given in the top panel, and  $^{12}\text{CO}(2-1)$  in the bottom. The top panel of Fig. 5 reveals regular circular rotation together with mild streaming motions in the molecular gas. However, the rough alignment of the molecular feature at  $\text{PA} \sim 88^\circ$  with the line-of-nodes of the galaxy ( $\text{PA} \sim 72 - 73^\circ$ , see Sect. 4) inhibits a clear signature of non-circular streaming motions. Consequently, the major-axis PV diagram cannot provide conclusive evidence for

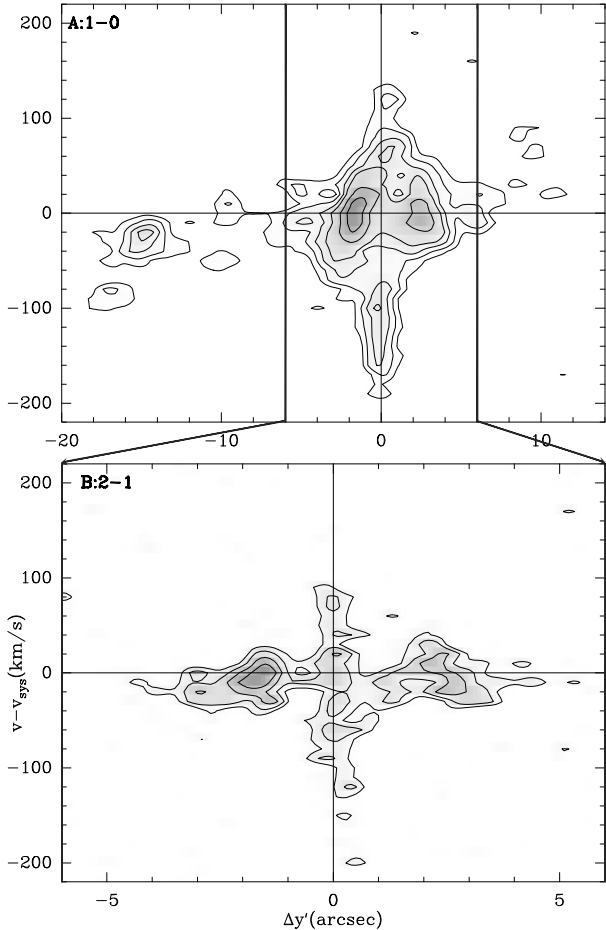


**Fig. 6.** Top panel: **a)** Position-velocity diagram of  $^{12}\text{CO}(1-0)$  along the kinematic minor axis of NGC 2782 (PA =  $165^\circ$ ) contoured over a grey-scale representation. Bottom panel: **b)** The same for  $^{12}\text{CO}(2-1)$ .

out-of-plane kinematics or for kinematic decoupling of the nuclear structure from the larger-scale stellar disk. The kinematics shown by the minor-axis PV in Fig. 6 are quite regular in the extended regions, but show significant velocity dispersion close to the nucleus. This could reflect an unresolved rotational velocity component, suggesting a large central dynamical mass (see below). Finally, Fig. 6 shows no evidence for molecular gas outflow, as tentatively suggested by Jogee et al. (1999).

### 3.3. The rotation curve and dynamical mass

We have derived a rotation curve (RC) from the PV diagram taken along the kinematic major axis of NGC 2782 at a PA =  $75^\circ$ . The terminal velocities were derived by fitting multiple Gaussian profiles to the spectra across the major axis. The fitted velocity centroids, corrected for  $\sin i$  ( $i = 30^\circ$ ), give  $V_{\text{rot}}$  for each galactocentric distance. Although for both lines the RCs to the south (nega-

tive velocities) are slightly steeper within the inner 300 pc than those to the north (positive), we averaged together the two curves derived from either side of the major axis. Hence, the resulting  $V_{\text{rot}}$  may be slightly shallower in the inner regions than the true mass distribution would imply. Because data for both lines were consistent, we combined both curves into an average by spline interpolation. The final RC is shown in Sect. 7.2 in the context of our numerical simulations.

The peak velocity is  $\sim 170/\sin i \text{ km s}^{-1}$ , or  $\sim 340 \text{ km s}^{-1}$  for  $i = 30^\circ$ , obtained at a radius of 850 pc ( $5''$ ) to the south, but at  $\sim 1 \text{ kpc}$  ( $\sim 6''$ ) in the RC obtained from averaging both lines and both sides of the major axis. From the peak velocity, we can derive a rough estimate of the dynamical mass:  $M(R) = 2.32 \times 10^5 R V^2(R)$  where  $M(R)$  is in  $M_\odot$ ,  $R$  in kpc, and  $V$  in  $\text{km s}^{-1}$ . Assuming the most flattened disk-like distribution (i.e., including a multiplicative constant of 0.6), at a radius of 1 kpc, we would find  $M_{\text{dyn}} = 1.6 \times 10^{10} M_\odot$ . Within a 1.7 kpc radius, where virtually all of the observed molecular gas is located, assuming a flat rotation curve (see Sect. 7.2), we would infer  $M_{\text{dyn}} = 2.7 \times 10^{10} M_\odot$ . Comparing with the mass in molecular gas including helium would give a molecular mass fraction of  $\sim 7\%$  in this region, in agreement with Jogee et al. (1999).

## 4. Stellar structure

Figure 7 shows the CO(1–0) and (2–1) total intensity maps overlaid on the IRAC  $3.6 \mu\text{m}$  image described in Sect. 2.1. This wavelength traces very well the massive component of the stellar populations in galaxies, and has the added advantage of very low extinction even compared to the  $K$  band. Two main inner structures can be seen in Fig. 7: an *inner stellar bar/oval* with a PA  $\sim 88^\circ$  and diameter of  $\sim 15''$ , and an *outer oval* at PA  $\sim 10^\circ$  and diameter of  $\sim 30''$ . Previous  $K$ -band observations (Jogee et al. 1999) identified similar features, but with slightly different PA's and a larger radius for the outer oval than we find here ( $25''$  vs.  $\sim 15''$ ). Both structures are clearly present in NGC 2782, and as we shall see in Sect. 6, contribute to the dynamical perturbations in this galaxy.

A large-scale view of NGC 2782 at  $3.6 \mu\text{m}$  is illustrated in (the left panel of) Fig. 8. The detached stellar sheet or tail outside the main galaxy disk is evident to the east, and the elongation or distortion of the disk to the west is clearly visible. There are also stellar arcs or “ripples” (Smith 1994; Jogee et al. 1999) about  $25''$  to the west of the nucleus. All these features are seen in optical images (Smith 1994; Jogee et al. 1999) and in HI (Smith 1991). Moreover, in HI, there is a long ( $\sim 54 \text{ kpc}$ ) plume or tidal tail extending to the north, with its origin at the westernmost edge of the distorted disk (Smith 1991).

<sup>2</sup> These values have been derived by fitting elliptical isophotes to the image with the task *ellipse* in the IRAF/STSDAS package.

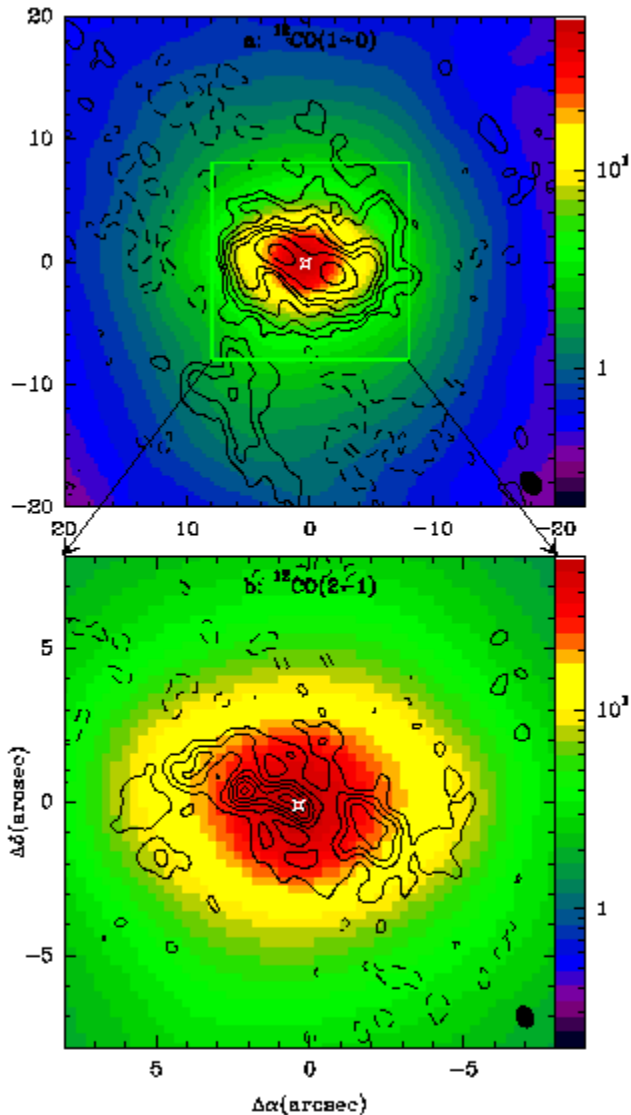


**Fig. 7.** Top panel: **a)**  $^{12}\text{CO}(1-0)$  total intensity contoured over a false-color representation of the IRAC  $3.6\ \mu\text{m}$  image of NGC 2782. The nuclear bar/oval and the outer oval can clearly be seen at  $\text{PA}\sim 88^\circ$  and  $\sim 10^\circ$ , respectively. Bottom panel: **b)** The same for  $^{12}\text{CO}(2-1)$ . In both panels, the AGN (dynamical center) position is marked with a star.

#### 4.1. Bulge/disk decomposition

To better understand the mass distribution and investigate the non-axisymmetric structure in the stars, we performed a two-dimensional bulge/disk decomposition on the IRAC  $3.6\ \mu\text{m}$  image of NGC 2782 with *galfit*, the publicly available algorithm developed by Peng et al. (2002). The MOPEX point-response function was used for convolution with the image, and the background sky level was fixed to the measured value rather than fit. Initial parameters for bulge and disk were guessed by using the scaling

relations given by Moriondo et al. (1998) and Hunt et al. (2004). The final best fit was achieved with a generalized exponential (Sersic) bulge, an exponential disk, and a nuclear point source.

We ran several sets of fits, in order to experiment with masking the stellar tails or sheets predominant to the east. Fitting the whole image ( $\sim 3.4'$  diameter) results in a bulge with shape index  $n = 3$  (a de Vaucouleurs bulge has  $n = 4$ ), an effective radius of 1.1 kpc and an apparent inclination of  $32^\circ$ . This bulge contains about 60% of the total  $3.6\ \mu\text{m}$  light. The resulting disk, with a scalelength of 2.9 kpc and an inclination of  $41^\circ$ , together with a nuclear point source contribute about 33% and 7%, respectively, to the total luminosity. The fitted aspect ratio of the disk is very close to that given for NGC 2782 in NED, which corresponds to a system inclination of  $42^\circ$ . The bulge PA of  $19^\circ$  is ill-determined because of its low apparent flattening, but the fitted orientation of the disk ( $\text{PA} = 73^\circ$ ) is consistent with the angle of the line-of-nodes estimated by Jogee et al. (1999) and with the kinematical major axis found in Sect. 3.2.

Masking the stellar “sheets”, and confining the fit to the undisturbed portion of the outer regions (within a  $\sim 2.4'$  diameter, 24 kpc) gives a slightly different, probably more reliable, fit. The bulge has a steeper shape index ( $n = 4$ ), the nuclear point source is smaller, and the disk is less inclined. The fraction of bulge-to-total luminosity remains the same,  $\sim 60\%$ . The masked fits give a disk inclination of  $33^\circ$ , more similar to that of the bulge, and more consistent with the visual aspect of the galaxy. Indeed, inspection of Fig. 8 suggests a strikingly round appearance, at least in the regular portion of the disk out to a radius of  $\gtrsim 50''$  ( $\sim 9$  kpc). This impression is confirmed by fitting the isophotes to ellipses<sup>3</sup> which shows that at galactocentric distances as large as 12.5 kpc, the fitted system ellipticity implies an inclination of  $\lesssim 33^\circ$  at  $\text{PA} = 72^\circ$ . Hence, we confirm  $\sim 30^\circ$  for the system inclination (as described in Sect. 3.2), obtained with the masked bulge-disk decomposition.

The fit provides a convenient axisymmetric model for unsharp masking. The large-scale residuals from the fit described above are shown in the right panel of Fig. 8. The correspondence with the features in the unsharp masked optical images (Smith 1994) is excellent. The stellar sheet to the east, and the ripples and distortion of the disk to the west, are clearly revealed. The small-scale residuals of the bulge/disk decomposition are shown in Fig. 9 with CO(1-0) (left panel) and CO(2-1) (right) overlaid in contours; both the “masked” fits and the fits to the entire image give virtually identical residuals in the circumnuclear region. The large ( $1''.2$ ) pixels of the IRAC image impede detailed comparison, but the residuals from the fit have an  $m = 2$  structure, and strongly resemble a stellar bar. Some small component of residuals could perhaps be hot dust

<sup>3</sup> With the task *ellipse* in the IRAF/STSDAS package.



rather than stars, because of the red  $K - L$  color excess observed in the center of NGC 2782 (Hunt & Giovanardi 1992). Nevertheless, dust cannot contribute significantly to the structure of the residuals because the  $K - L$  color is redder outside the bar-like structure than within it. In fact, the position of the bar-like residuals coincides perfectly with the CO emission, and provides a classic illustration of the theoretical behavior of the spiral response of a gas component to bar forcing. In this case, the gas is phase shifted in advance relative to the bar (leading), as can be seen to the northeast and the southwest in the “S” shape of the spiral.

## 5. Star formation and dust in NGC 2782

While stellar structure can be more readily inferred from near-infrared (NIR) wavelengths, dust extinction and star formation are best investigated in the optical. Figure 10 shows the CO intensity maps overlaid on the HST/WFPC2 F814W image. The F814W emission of the circumnuclear region shows a strong asymmetric excess to the northwest of the AGN (hereafter called the “NW excess”), roughly coincident with the structure in the  $H\alpha$  maps (Jogee et al. 1999). This excess is contiguous with an entire arc of bright knots to the north running from east to west, again reflecting the  $H\alpha$  emission-line morphology. Part of this arc lies within the  $^{12}\text{CO}(2-1)$  emission, while the excess to the northwest is outside of it. There is also an extended F814W excess generally to the south, leading to a lopsided appearance at this wavelength.

Figure 11 presents the CO intensity maps overlaid on the HST/WFPC2  $V - I$  image described in Sect. 2.1. The red  $V - I$  color delineating the spiral arm to the northwest is neatly traced by the CO(1-0) emission. This red arm connects to the CO spiral with a hook-like structure which winds around the NW excess, following the CO emission to the nucleus. The blue  $V - I$  colors of the F814W arc to the north of the AGN suggest that it is tracing the same star-formation episode revealed by  $H\alpha$ .

This northern arc of star formation was identified by Jogee et al. (1998) and Jogee et al. (1999), and occurs roughly cospatially with an outflow thought to be driven by the starburst. The outflow is seen at radio wavelengths and in optical emission lines (Boer et al. 1992; Saikia et al. 1994; Jogee et al. 1998; Yoshida et al. 1999; Jogee et al. 1999). It is relatively north-south symmetric in the 6 cm radio continuum (Saikia et al. 1994), but has the form of a “mushroom” in the optical (clearly illustrated by Fig. 8 in Jogee et al. 1999). The arc defines the “cap” of the mushroom, and the slightly narrower “stem” extends southward, ending at the blue knot roughly  $\sim 7''$  south and  $1''$  east of the nucleus. This mushroom shape is not clearly seen in the  $V - I$  image. The roughly normal  $V - I$  colors ( $\sim 0.8-1$ ) to the south of the CO(2-1) emission suggest that the unreddened stellar population

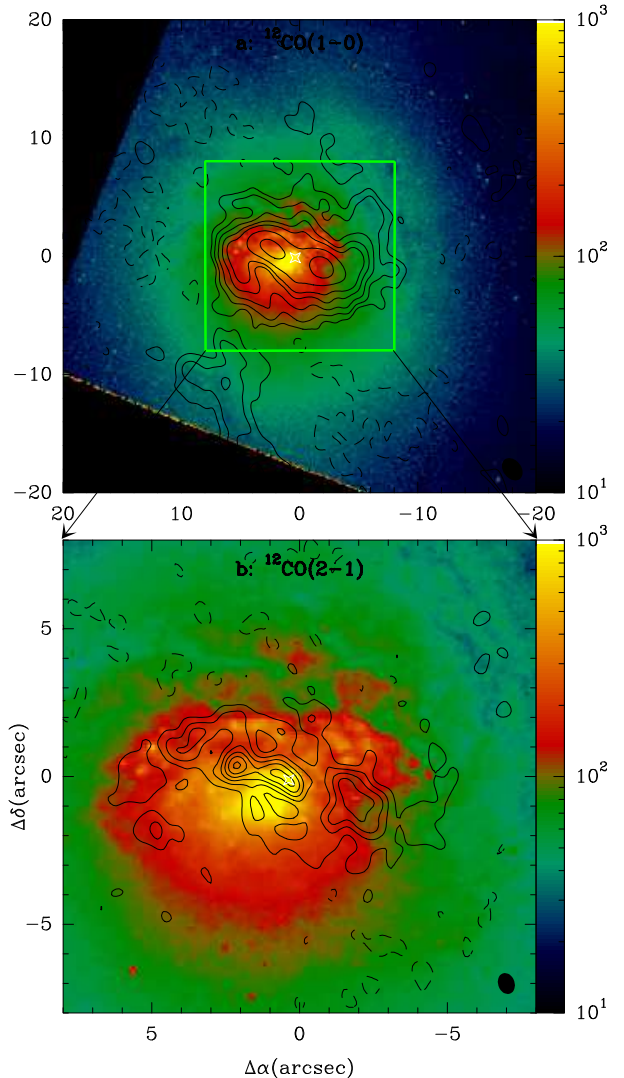


**Fig. 10.** Top panel: **a)**  $^{12}\text{CO}(1-0)$  total intensity contoured over a false-color representation of the HST/WFPC2 F814W image of NGC 2782. Bottom panel: **b)** The same for  $^{12}\text{CO}(2-1)$ . In both panels, the AGN (dynamical center) position is marked with a star.

of the bulge is obscuring the star formation to the south, a conclusion which we will motivate in the following.

The three-dimensional orientation of the galaxy disk can be inferred on the basis of the red  $V - I$  colors in the extended spiral arm in the northwest. The roughly symmetric spiral arm to the southeast is not reddened, implying that the spiral structure to the northwest is being seen through an obscuring dust lane, coplanar with the inclined stellar disk. If this is true, then the north would be the near side of the disk, and the south would be the far side. This orientation would also mean that the spiral arms are trailing, which is the most probable configuration. The implication is that, toward the south, the stellar disk is seen through the intervening bulge. The rel-



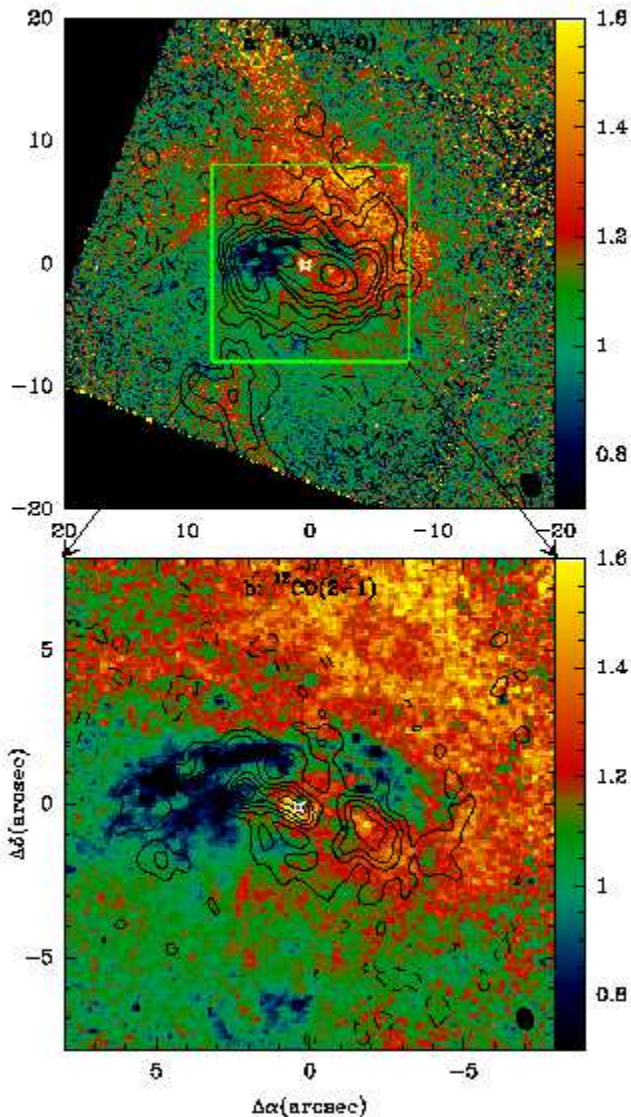


**Fig. 11.** Top panel: **a)**  $^{12}\text{CO}(1-0)$  total intensity contoured over a false-color representation of the HST/WFPC2  $V - I$  image of NGC 2782. The spiral arm to the northwest is clearly traced by the CO(1-0) emission. Bottom panel: **b)** The same for  $^{12}\text{CO}(2-1)$ . In both panels, the AGN (dynamical center) position is marked with a star.

atively small bulge effective scalelength of  $5''-6''$  means that  $\sim 50\%$  of the bulge light lies within the region of the CO emission. To the south, the bulge stars with normal  $V - I$  colors are overwhelming the young blue stars in the star-formation event. Hence, the southern part of the “mushroom” structure is not observed in  $V - I$ , but in emission lines, since the bulge is not expected to contain a significant amount of dust, nor does it emit contaminating line emission. To the south most of the bulge is in

front of the intervening dust lane, while to the north, dust obscures more of the bulge because most of the bulge light is behind it. This interpretation would also help explain the F814W image with its apparent lopsidedness to the south. In any case, the dust must be clumpy, and inhomogeneities in the dust distribution allow random regions behind the dust to shine through.

The AGN (dynamical center) is located at the north-west border of a tiny red arc  $\sim 80$  pc to the south-east (“parachute”-like, see Fig. 11). In this region, there are broad H $\alpha$  lines which show considerable north-south asymmetry, unlike the narrow component of the emission lines which is relatively symmetric (Yoshida et al. 1999). Interestingly, this red arc in the color map is at the same position as the velocity discontinuities in the CO(2-1) spider diagrams (see Sect. 3.2). Because of the feature’s extremely small size, we can not make any reliable statements, but speculate that it could be the color (and kinematic) signature of a small-scale AGN outflow out of the plane of the disk.

## 6. Gravitational torques on the molecular gas

Streaming motions along the bar led Jogee et al. (1999) to conclude that there could be gas inflow feeding the starburst. However, streaming motions by themselves do not imply any transfer of angular momentum, nor can they be used to infer the direction of such transfer. Hence, we now examine the torques exerted by the stellar potential on the molecular gas in NGC 2782, in order to assess whether the gas is, on average, flowing in or out. Although our PdBI map recovers  $\sim 65\%$  of that from single-dish measurements, in the following analysis what matters is the structured gas component. The diffuse large-scale molecular gas contributes equal quantities of positive and negative torques on the gas orbits; hence it does not influence the net torque.

There is no clear evidence for non-coplanarity of the CO nuclear bar+spiral and the large-scale stellar disk. The stellar bar is oriented at  $\text{PA} \sim 88^\circ$ , and the kinematic major axis at  $\sim 75^\circ$ , somewhat hampering the identification of non-circular motions. Nevertheless, were the two structures to be non-coplanar, we would expect to see some kinematic evidence which is not seen. Hence, in disagreement with the schematic model presented by Yoshida et al. (1999), in what follows, we assume that all the flattened structures (nuclear CO spiral, nuclear stellar bar, and outer stellar oval) lie within the same disk plane.

To derive the torques exerted by the stars on the gas, we adopt the method presented in García-Burillo et al. (2005) which relies on a stellar potential  $\Phi$  derived from a NIR image and on the gas response as inferred from the CO maps. We assume that the total mass is determined by the stars, essentially invoking an extreme “maximum disk” solution (e.g., Kent 1987), in which the gas self-gravity and the dark matter halo are neglected. We fur-

then assume that the measured gas column density  $N(x, y)$  derived from the CO total intensity maps is a reliable estimate of the probability of finding gas at  $(x, y)$  in the current epoch. This is reasonable, namely that CO traces the total gas content, since atomic gas in the nuclei of galaxies is typically a very small fraction of the total gas mass.

As emphasized in García-Burillo et al. (2005), a single key assumption underlies the validity of our estimate of angular momentum transfer in the gas: we implicitly assume that the gas response to the stellar potential is roughly stationary in the reference frame of the potential over a few rotation periods. This would not be the case in the presence of strong self-gravity in the gaseous components. However, otherwise, even in galaxies with several stellar pattern speeds at different radii in the disk, numerical simulations suggest that the gas response adjusts its response to the dominant stellar configuration at a given radius (see García-Burillo et al. 2005, and references therein).

### 6.1. The stellar potential

The stellar potential in NGC 2782 was derived from the IRAC 3.6  $\mu\text{m}$  image by first rebinning to  $0''.15$  pixels, then deprojecting with a PA =  $75^\circ$  and an inclination of  $30^\circ$ . To account for the vertical mass distribution, the rebinned deprojected image was convolved with an isothermal plane model of constant scale height  $\sim 1/12$ th of the radial disk scalelength (e.g., Quillen et al. 1994; Buta & Block 2001). Figure 12 shows the deprojected IRAC image, with the  $^{12}\text{CO}(1-0)$  and  $^{12}\text{CO}(2-1)$  total intensity maps superimposed in contours. The orientations of the stellar outer oval and the nuclear oval/bar are clearly visible even in the deprojected image and are marked with a solid line.

In the absence of extinction and stellar population gradients, the mass-to-light ratio can be assumed to be constant across this deprojected (face-on) galaxy image (e.g., Freeman 1992; Persic et al. 1996); the mass is therefore directly proportional to the 3.6  $\mu\text{m}$  light distribution. With this assumption, we derive the potential  $\Phi$  by solving the Poisson equation:  $\Delta\Phi = 4\pi G\rho$  using a Fast Fourier Transform (FFT) technique on a  $256 \times 256$  Cartesian grid as in Combes et al. (1990). Beyond a radius of 3.4 kpc,  $\rho$  is set to 0, thus suppressing any spurious  $m = 4$  terms in the derived potential. This is adequate to compute  $\Phi$  in the central regions of the galaxy sampled by the PdB CO(1-0) primary beam.

Following Combes & Sanders (1981), we then expand the potential  $\Phi$  in Fourier components:

$$\Phi(R, \theta) = \Phi_0(R) + \sum_m \Phi_m(R) \cos[m(\theta - \theta_m)] \quad (1)$$

and use a polar Fourier transform method to isolate the various angular modes  $\Phi_m$ . It is convenient to represent

each  $m$ -Fourier amplitude by the normalized ratio  $Q_m(R)$ :

$$\begin{aligned} Q_m(R) &= \frac{m}{R} \Phi_m(R) / \left( \frac{\partial \Phi_0(R)}{\partial R} \right) \\ &= m \Phi_m / R |F_0(R)| \end{aligned} \quad (2)$$

which is the amplitude of the  $m^{\text{th}}$  harmonic of the force relative to the total axisymmetric component. These are essentially the harmonics of the angular derivatives of the potential, expressed as normalized Fourier amplitudes. Figure 13 gives the radial run of the highest-order  $Q_m(R)$  coefficients. The nuclear ( $R \simeq 1$  kpc) and the primary ( $R \simeq 2.6$  kpc) bars are clearly evident as local maxima (see left panel); moreover, the phase angle changes as would be expected for the  $\sim 90^\circ$  transition from the nuclear to the primary bar ( $Q_2$  shown as a solid line, right panel).

### 6.2. Derivation of the torques

The angular derivative of the potential  $\Phi(R, \theta)$  gives at each location the torque field per unit mass  $\tau(x, y) = xF_y - yF_x$ ; by definition  $\tau(x, y)$  is independent of the gas distribution in the plane of the galaxy. The azimuthal average of  $\tau$ , using  $N(x, y)$  as the weighting function, corresponds to the global variation of the specific gas angular momentum transfer occurring at this radius ( $dL_s(x, y)/dt|_\theta$ ). The  $\theta$  subscript indicates an azimuthal average, evaluated at a given radius  $R(x, y)$ . For convenience of calculation on a pixelized image, we express the torques in Cartesian coordinates.

The rotation direction of the gas in the galaxy disk determines the sign of  $\tau(x, y)$ : positive (negative) if the torque drives the gas outward (inward) at  $(x, y)$ . To calculate the effective variations of angular momentum in the galaxy plane, we then weight the torques by the gas column densities  $N(x, y)$  derived from the  $^{12}\text{CO}(1-0)$  and 2-1 lines:  $\tau(x, y)N(x, y)$ . Fig. 14 shows the normalized version of these maps  $\tau'$  where we have divided  $\tau(x, y)N(x, y)$  by the azimuthal average of the gas density. The  $'$  superscript indicates this normalized  $\tau$ , so that we can use dimensionless quantities (both in Cartesian coordinates and below in polar ones). Both panels in Fig. 14 show the typical “butterfly” diagram due to an  $m = 2$  perturbation (e.g. Buta & Block 2001; Laurikainen & Salo 2002).

The radial gas flow induced by the torques is estimated by azimuthally averaging the effective variations of angular momentum density in the plane:

$$\tau'(R) = \frac{\int_\theta N(x, y) \times (x F_y - y F_x)}{\int_\theta N(x, y)} \quad (3)$$

$\tau'(R)$ , by definition, represents the azimuthally-averaged time derivative of the specific angular momentum  $L_s$ . Azimuthal averages are derived with a radial binning commensurate with the  $1''.2$  resolution of the IRAC image. Similarly to the torque maps (e.g., Fig. 14), the sign of

$\tau'(R)$  defines whether the gas is subject to a net gain (+) or loss (−) of angular momentum. Specifically, we assess the efficiency of the AGN fueling by estimating the average fraction of the gas angular momentum transferred in one rotation period by the stellar potential. This is done as a function of radius by defining the dimensionless function  $\Delta L/L$ :

$$\frac{\Delta L}{L} = \frac{dL}{dt} \Big|_{\theta} \times \frac{1}{L} \Big|_{\theta} \times T_{rot} = \frac{\tau'(R)}{L_{\theta}} \times T_{rot} \quad (4)$$

where  $T_{rot}$  is the rotation period, and  $L_{\theta}$  is assumed to be well represented by its azimuthal average, i.e.,  $L_{\theta} = R \times v_{rot}$ . The absolute value of  $L/\Delta L$  dictates how much time the stellar potential will need to transfer the entirety of the total gas angular momentum. Assuming that the gas response to the stellar potential is stationary with respect to the potential reference frame during a few rotation periods, a small value of  $\Delta L/L$  implies that the stellar potential is inefficient at present. Figure 15 shows the  $\Delta L/L$  relative torques derived from CO(1–0) (top panel) and 2–1 (bottom). Because of the limited resolution in the IRAC image (1 pixel  $\simeq$  200 pc), we have masked the inner pixel. Beyond a radius of  $\sim 1.9$  kpc, the  $^{12}\text{CO}(2-1)$  emission is less well sampled than  $^{12}\text{CO}(1-0)$  because of the smaller beam size ( $\sim 22''$ ). The two CO lines are thus complementary, as  $^{12}\text{CO}(1-0)$  effectively traces the torques beyond this radius, but at a more moderate spatial resolution than  $^{12}\text{CO}(2-1)$ . It is evident that both lines give similar results, in the sense that we see *systematically negative average torques in the inner few kpc*.

## 7. Understanding the torques in NGC 2782

The other galaxies in the NUGA sample analyzed so far (García-Burillo et al. 2003; Combes et al. 2004; García-Burillo et al. 2005; Boone et al. 2007) mainly show positive torques near the nucleus, with negative torques at varying amplitudes only for radii  $\gtrsim 500$  pc. Only in NGC 4579 are the average torques negative down to 200 pc, but the spatial resolution of the torque map for that galaxy is sufficiently good that we can see that, inside that radius, the gas is flowing *away* from the nucleus. NGC 2782 is the first galaxy in our sample that shows systematically negative torques down to the resolution limit imposed by our torque image. Moreover, in the entire region probed by our CO maps, nowhere is the gas subjected to average positive torques. The relatively poor resolution ( $1''.2$ ) of the potential map (IRAC  $3.6 \mu\text{m}$ ) makes it impossible to assess the torque amplitude inside a radius of  $200 \text{ pc}^4$ . Indeed, the slightly positive torques in Fig. 15 are unreliable, and may simply be an artefact of insufficient

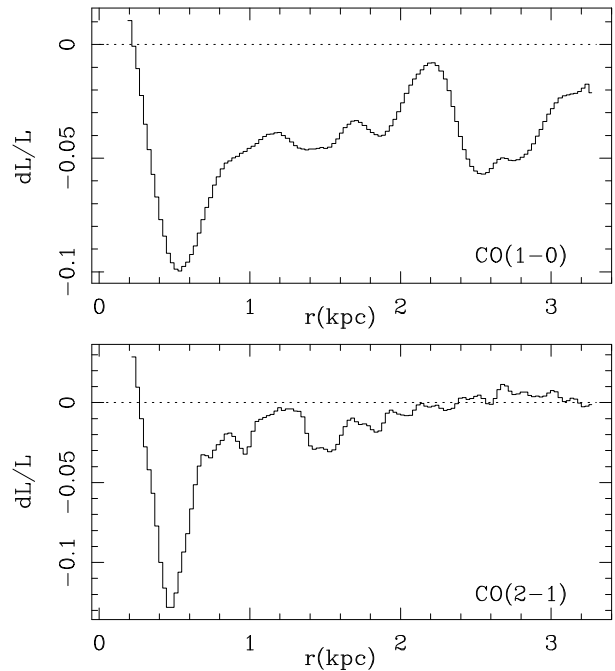


**Fig. 15.** Top panel: **a)** The relative torque in dimensionless units of  $dL/L$  derived using the potential obtained from the *Spitzer*/IRAC  $3.6 \mu\text{m}$  image ( $1.2''$  pixels, under-sampled beam). Bottom panel: **b)** The same for  $^{12}\text{CO}(2-1)$ . The  $^{12}\text{CO}(2-1)$  emission is less well sampled than  $^{12}\text{CO}(1-0)$  beyond a radius of  $\sim 1.9$  kpc, because of the smaller beam size (FWHP  $\sim 22''$ ). Despite the relatively poor resolution of the gravitational potential image, both CO transitions give similar results; we see *systematically negative average torques within the entire region probed by our observations*.

spatial resolution. Nevertheless, the systematically negative trend of the average torques in NGC 2782 hints that gas is being transported tantalizingly close to the AGN. This gas is certainly fuelling the nuclear starburst, and may, subsequently, be feeding the AGN. In the following, we develop a dynamical scenario which will explain why we think this occurs in NGC 2782.

### 7.1. Main features

Although the outer parts of NGC 2782 show clear signs of a past interaction (tidal tails, distorted disk, stellar sheets), the inner parts appear dynamically relaxed, not unexpectedly since the dynamical timescale is shorter by one or two orders of magnitude at  $r \sim 1 \text{ kpc}$ , than at  $r \sim 20 \text{ kpc}$ .

The previous sections have shown that NGC 2782 contains many features of a double-barred galaxy. Although the nuclear bar is unfortunately almost aligned with the galaxy line of nodes, the disk is nearly face-on ( $30^\circ$ ), which helps to distinguish the morphological features. In the

<sup>4</sup> As in García-Burillo et al. (2005), we attempted to use the *HST* WFPC2 F814W image corrected for extinction. However, in NGC 2782, the extinction correction proved to be unreliable, and we were forced to rely only on the *Spitzer*/IRAC image.

near-infrared, there is a nuclear stellar bar of radius  $\sim 1$  kpc, embedded within an outer stellar oval of radius  $\sim 2.5$  kpc. This outer oval, which we will call the primary bar, is oriented at PA  $\sim 10^\circ$ , misaligned (and not quite perpendicular) with the nuclear stellar bar at PA  $\sim 88^\circ$ . The molecular gas distribution is mainly elongated along the nuclear bar, and reveals two spiral features emerging from its ends, aligned with the conspicuous dust lanes already noted by Jogee et al. (1998, 1999). These dust lanes are strikingly straight, reminiscent of barred galaxies with dust lanes parallel to the bar, but located on the bar’s leading edge on either side of the nucleus. We therefore interpret the large-scale CO(1–0) features corresponding to the straight dust lanes as the gas response to the primary bar; they have indeed a similar orientation. The inner elongated molecular morphology, evident in both CO(1–0) and CO(2–1), constitutes the gas response to the nuclear bar.

The H $\alpha$  morphology is more puzzling, because of a clumpy dust obscuration which masks part of it. As noted by Jogee et al. (1998), there are two main features in H $\alpha$ : one is the outflow driven by the starburst, perpendicular to the nuclear stellar bar, and aligned with the radio continuum outflow (Saikia et al. 1994), and the other is the elongated ring, of about 1 kpc in radius, encircling the nuclear bar. The ring is particularly demarcated on the northern side, where it forms a  $180^\circ$  arc, making the structure resemble more a half-ring or what we called the “cap of the mushroom” in Sect. 5. But there is also a southern equivalent (dubbed the “mushroom stem”), largely obscured by dust. Toward the west, there is a remarkable dust finger, devouring the ring, which superposes quite well with the CO distribution (see Fig. 11).

The two different H $\alpha$  components are well distinguished by their different kinematics: large outflowing velocities in the north-south component (bubble to the south in front of the dust lane, and obscured flow in the north behind it), and a normally rotating ring around the nuclear bar (Yoshida et al. 1999). We interpret the low-velocity rotating component as the nuclear ring, associated with the inner Lindblad resonance (ILR) of the primary bar, and encircling the nuclear bar, i.e. close to the corotation (CR) of the nuclear bar (more exactly at the UHR, or 4:1 resonance). The dust features are more conspicuous toward the north because the near side is the north side. The bulge is more evident toward the south, masking the dust obscuration from the disk’s far side. But this does not imply that there is no dust and gas there, obscuring the southern half-ring in H $\alpha$ : on the contrary, there is CO emission in this southern part, coinciding with holes in the H $\alpha$  distribution.

The H $\alpha$  emission is the most intense in the partial ring, which lends support to our ILR interpretation, since it is well-known that resonances are locations where the gas is transiently stalled due to the torques provided by the stellar bar. Thus, the gas has time to form young stars, as typically revealed in many barred galaxies, such

as NGC 2997, NGC 4314, or NGC 4321 (Maoz et al. 1996; Benedict et al. 2002; Allard et al. 2006). In the case of NGC 2782, because of the secondary bar, gas is then driven further inward, as suggested by the CO straight spiral arms (pitch angle close to  $90^\circ$ ) aligned with the nuclear bar. This gas also forms stars, explaining the presence of H $\alpha$  also in the nuclear disk.

## 7.2. Dynamical interpretation

The dynamical scenario we propose to explain these main features is the following: first a primary bar forms, most likely triggered by the interaction that gave rise to the disturbed morphology in the outer parts of NGC 2782. The gravity torques from this primary bar drive the gas inward, and create a gaseous nuclear ring at its ILR. Intense star formation gives rise to the H $\alpha$  nuclear ring, seen now as a sharp half-ring arc. In the meantime, the gas inflow has weakened the primary bar (e.g., Bournaud & Combes 2002; Bournaud et al. 2005), and a nuclear bar has dynamically decoupled, rotating at a different pattern speed. The two different pattern speeds are usually such that the corotation of the nuclear bar corresponds to the ILR of the primary bar, thus avoiding excessive chaos in the orbits (Friedli & Martinet 1993). The nuclear bar then governs the gas inflow toward the center. Instead of being stalled at the primary ILR, now the gas is subject to the negative gravity torques of the secondary bar, between its CR and its own ILR. This explains why we see CO emission inside the ILR of the primary bar, and why the torques computation reveals that gas is flowing inward toward the center.

This scenario is slightly different from one where the gas decouples from the stars to form a gaseous nuclear bar with a faster (Englmaier & Shlosman 2004) or slower (Heller et al. 2001) pattern speed than the primary bar. We propose here that the nuclear bar exists both in the stellar and gaseous components, and always with a higher pattern speed than the primary.

## 7.3. Numerical techniques

To better understand the physical mechanisms, and reproduce the observed morphology, we performed N-body simulations with stars and gas, including star formation. We believe that the nuclear bar decoupling is a disk phenomenon, occurring on short timescales, with little contribution of a slowly rotating spherical component, such as a bulge or dark matter halo, so we adopt the simplification of 2D simulations, with the spherical components added analytically. Self-gravity is included only for the disk (gas+stars).

The N-body simulations were carried out using the FFT algorithm to solve the Poisson equation, with two kinds of grids: Cartesian and polar, the latter optimizing the spatial resolution toward the center. The useful

Cartesian grid was  $256 \times 256$  (or  $512 \times 512$  in total to avoid periodic images), with a total radius of 8 kpc. The cell size is then 62 pc. The softening was taken as 250 pc, in order to roughly reproduce the actual effective softening from the thickness of the disk. The polar grid is composed of  $NR = 80$  radial, and  $NT = 96$  azimuthal separations. The radial spacing of the grid is exponential at large scales, and linear at small scales, following the prescription by Pfenniger & Friedli (1993). The polar-grid cell size ranges from 10 pc at the center to  $\sim 1$  kpc at the outskirts (at 22 kpc). The minimum softening is also fixed at 250 pc, and is larger in the outer regions. The two different kinds of simulations, polar and Cartesian, were performed separately, in order to gauge the effect of different spatial resolution on the results; both methods give similar outcomes.

The stellar component is represented by 120000 particles, and the gas component by 40000. Two rigid spherical potentials are added analytically, with a Plummer shape:

$$\Phi_{b,h}(r) = -\frac{GM_{b,h}}{\sqrt{r^2 + r_{b,h}^2}}$$

where  $M_b$  and  $r_b$  are the mass and characteristic radius of the stellar spherical component (bulge), and  $M_h$  and  $r_h$  are the equivalent quantities for the dark-matter halo. These parameters are selected to fit the rotation curve of NGC 2782, and are reported in Table 1.

The stellar disk is initially a Kuzmin-Toomre disk of surface density:

$$\Sigma(r) = \Sigma_0(1 + r^2/r_d^2)^{-3/2}$$

with mass  $M_d$ ,  $r_d = 3.25$  kpc, and truncated at 7 kpc. It is initially quite cold, with a Toomre  $Q$  parameter of 1.2. The gas distribution is initially similar to the stellar one, with  $Q_{gas} = 1$ . The time step is 0.1 Myr. The initial conditions of the runs described here are given in Table 1. The component subscripts refer to the bulge ("b"), and the halo ("h") which are rigid, and the disk ("d") which is "live".

**Table 1.** Initial conditions parameters

Run	$r_b$ kpc	$M_b$ $M_\odot$	$M_d$ $M_\odot$	$M_h$ $M_\odot$	$F_{gas}$ %
Run A	0.2	2.3e10	1.4e11	4.5e10	10
Run B	0.5	2.3e10	9.0e10	9.0e10	10
Run C	0.2	2.3e10	1.4e11	4.5e10	5
Run D	0.5	2.3e10	9.0e10	9.0e10	5

All masses are given inside 7 kpc radius;  $r_d$  and  $r_{gas}$  are fixed at 3.25 kpc, and  $r_h$  at 7.5 kpc.

The gas fraction  $F_{gas}$  is the fraction of the total mass (halo included).

The gas is treated as a self-gravitating component in the N-body simulation, and its dissipation is treated by a sticky particle code, as in Combes & Gerin (1985). The initial gas-to-total mass ratio ( $F_{gas}$ ) ranges between 5 and 10%. Star formation is included, with a conventional Schmidt-law recipe, although this will not be discussed here, since the timescales are short enough that the gas depletion is not significant. At the present time, the observed gas mass in NGC 2782 within a  $\sim 3$  kpc radius is about  $3 \times 10^9 M_\odot$ . The gas clouds are subject to inelastic collisions, with a collision cell size of 67 pc for the Cartesian code, and 117 pc for the polar code (region where particles are selected to possibly collide). This corresponds to a lower limit for the average mean free path of clouds between two collisions. The collisions are considered every 2 Myr. In a collision, the sign of the relative cloud velocities is reversed and the absolute values are reduced: relative velocities after the collision are only 0.65 times their original value. The dissipation rate is controlled by this factor. All gas particles have the same mass.

The rotation curve corresponding to Run A is plotted in comparison to the empirical RC (see Sect. 3.3) in Fig. 16. All other runs have similar rotation curves. In the figure, we show the circular velocity  $V_{circ}$  deduced from the potential ( $d\Phi/dr = V_{circ}^2/r$ ). In the range of 200–800 pc, there are non-circular streaming motions (see Sect. 3.2) which contribute to the derived empirical  $V_{rot}$ . Indeed, we have calculated  $V_{rot}$  of the gas from the model, azimuthally averaged at a given radius, and find streaming motions of amplitude similar to the observed discrepancies between the empirical RC as traced by CO and the predicted  $V_{circ}$ . Given the uncertainties, and the asymmetry of the two sides of the major axis (see Sect. 3.3), all theoretical curves are compatible with the empirical ones. The data points for the epicyclic frequency resonances, marked by  $\times$  and  $+$  in Fig. 16, are calculated by numerically differentiating the smoothed empirical RC. These data are also generally compatible with the predictions of the numerical simulations.

#### 7.4. Simulation results

Several runs have been carried out in order to test the various parameters, and evaluate the dependence of the results on the central mass concentration and on the initial gas mass fraction. These parameters are crucial for the nuclear bar decoupling. Only four of these models are displayed in Table 1.

We found that a high central mass concentration was necessary to decouple the secondary bar, as already shown by Friedli & Martinet (1993). This can be understood be-

<sup>5</sup> As derived from the short-spacing single-dish observations of Young et al. (1995), see Sect. 3.1.

<sup>6</sup> As noted in Sect. 3.3, the unfortunate coincidence of the PA of the bar and the disk line-of-nodes makes streaming signatures difficult to diagnose in PV and isovelocity diagrams.



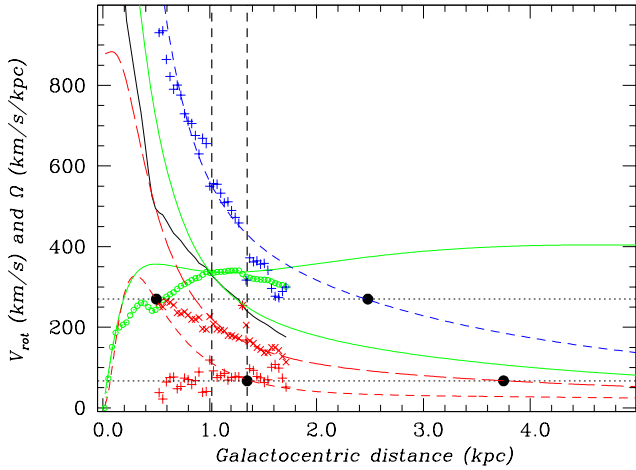


**Fig. 16.** Rotation and derived frequency curves  $\Omega$ ,  $\Omega - \kappa/2$  and  $\Omega + \kappa/2$  adopted for the simulations (Run A), together with the empirical curves derived from the CO(2–1) and (1–0) PV diagrams. The (green) open circles trace the empirical  $V_{\text{rot}}$ , coinciding with theoretical circular velocity  $V_{\text{circ}}$  (traced by a solid line) at  $R=1$  kpc and at small radii. The remaining solid lines are the empirical (black) and theoretical (green)  $\Omega$  curves. The long-dashed line is the  $\Omega - \kappa/4$  curve, and the short-dashed ones are the  $\Omega \pm \kappa/2$  ones. The corresponding data points are shown as  $\times$  and  $+$ ; the data have been masked within 500 pc to minimize confusion. The two pattern speeds inferred from the simulations are shown as horizontal dotted lines, and resonances are marked with filled circles. The vertical dashed lines correspond to the nuclear bar length ( $\sim 1$  kpc) and the ILR of the outer oval ( $\sim 1.3$  kpc), also roughly equal to the nuclear bar’s CR at  $\sim 1.1$  kpc. The apparent mismatch of the empirical and theoretical RCs, in the range of 200–800 pc, is due to non-circular streaming motions (Sect. 3.2) and asymmetry in the two sides of the rotation curve (Sect. 3.3) which contribute to the inferred average  $V_{\text{rot}}$ .

cause the two pattern speeds are close to the precessing rates of the supporting orbits, which are traced by the  $\Omega - \kappa/2$  curve. A high mass concentration produces a marked maximum of this curve in the center, with a large radial gradient favorable to the decoupling. Also, a high gas mass fraction of at least 5% of the total mass is required for the decoupling. The nuclear bar is even stronger with a gas fraction of 10%. In Run B and D, with a scale-length of the bulge twice that of Run A and C, the mass concentration was not enough to produce the decoupling of the nuclear bar.

Run A, with a small bulge scalelength, and a high gas mass fraction, provides the best fit for NGC 2782. The stellar and gaseous morphologies are displayed in Fig. 17 at three epochs, shortly after the second bar decoupling.

As seen in Fig. 17, between  $\sim 700$  and 750 Myr the gas is inflowing. Moreover, the gas is always “leading” the stars, and thus is slowed down by them.

The Fourier analysis of the gravitational potential during the decoupling of the two bars clearly shows the development of the two modes. The Fourier analysis has been performed as a function of radius, every 2 Myr, during 100 Myr in this period. The Fourier transform of the results over the time axis gives the pattern speed as a function of radius, as shown in Fig 18, with a resolution in  $\Omega_p$  of  $30 \text{ km s}^{-1} \text{ kpc}^{-1}$ . Of necessity, the temporal averaging must be performed over the lifetime of the transient features; this averaging “thickens” the value of  $\Omega_p$  in the plot because of the time variation of the pattern speed of the nuclear bar.

Figure 18 lets us unambiguously isolate two bars in the potential, dominated by the stellar component:

- The nuclear bar with  $\Omega_b \sim 270 \text{ km s}^{-1} \text{ kpc}^{-1}$ . Its corotation is at about 1.1 kpc, at a radius just slightly larger than its size of 1 kpc.
- The primary bar with  $\Omega_b \sim 65 \text{ km s}^{-1} \text{ kpc}^{-1}$  and an ILR at  $\sim 1.3$  kpc, roughly coincident with corotation of the nuclear bar; the primary bar CR is at  $\sim 5$  kpc, and its UHR at  $\sim 3.6$ – $3.8$  kpc. In the gas morphology, there is a (pseudo) inner ring coinciding with the UHR resonance (see Fig. 17).

From these identifications, we can interpret the elongated nuclear ring as the ILR of the primary bar at  $R \sim 1$  kpc, coinciding with the UHR/CR of the nuclear bar. This ring corresponds to the H $\alpha$  arc, or half-ring, encircling the NIR nuclear stellar bar. Inside the ILR ring (of the primary bar), the gas morphology reveals two spiral arms with large pitch angle, now aligned with the nuclear bar. These gas arms are leading with respect to the stellar bar, and this phase shift means that the gravity torques from the stars are negative, driving the gas inward. These arms are winding up in a ring around the center, which corresponds to the ILR of the nuclear bar. Indeed, it can be seen from the frequency curves in Fig 16 that the pattern speed of the secondary bar ( $270 \text{ km s}^{-1} \text{ kpc}^{-1}$ ) crosses the  $\Omega - \kappa/2$  curve at about  $300 \text{ pc}^7$ . The two arms aligned along the nuclear bar can be identified with the CO features, observed with the interferometer. There is also a hole in the center in the gas distribution, which could correspond to the ILR of the nuclear bar.

<sup>7</sup> Indeed, the high maximum of the  $\Omega - \kappa/2$  curve is certainly overestimated by the epicyclic approximation, since the orbits are very elongated. Hence, although in our simulations,  $\Omega_p$  of the secondary bar would indicate two ILRs, it is more likely that there is only a single ILR, roughly in the middle at  $\sim 200$  pc.



### 7.5. Decoupled bars: gas infall in NGC 2782

The previous simulations, adapted to the rotation curve of NGC 2782, support the scenario proposed in section 7.1. A primary bar, perhaps triggered by the past interaction, has driven gas toward its ILR, and while this bar was weakening, a secondary embedded bar has decoupled, prolonging the gas inflow inside the ILR ring, which is now conspicuous in star formation and  $H\alpha$  emission. The gas has been driven into two spiral arms, aligned with the nuclear bar, and is now winding up to the ILR of the nuclear bar, i.e. at about 200–300 pc radius. This scenario allows a coherent interpretation of the low-velocity  $H\alpha$  component and the entire CO morphology, as well as of our finding of negative gravity torques. In NGC 2782, there seems to be a “smoking gun”, namely the presence of molecular gas inside the ILR of the primary bar, made possible by the decoupling of a secondary nuclear bar from the primary one. The gas there is certainly fueling the central starburst, at the origin of the ionized gas bubble, and in a second step should fuel directly the AGN. The timescales in this central region are quite short, about 6 Myr for the gas rotation period at 300 pc. Dynamical friction and viscous torques can then relatively quickly provide gas to fuel the AGN (García-Burillo et al. 2005, 2007), although the present simulations do not have enough spatial resolution to simulate that realistically. Alternatively, the ILR of the nuclear bar suggested by our models could impede further gas inflow inside the resolution limit of our images.

According to our simulations, there are two salient characteristics of NGC 2782 which lead to the secondary bar decoupling, and the ensuing negative torques. The first is its conspicuous stellar bulge, as suggested by the bulge-disk decomposition described in Sect. 4.1. This is the biggest contributor to the central mass concentration, and the likely cause of the resonances that give rise to the gas buildup in the rings, with the subsequent decoupling of the secondary nuclear bar. The second feature is the particularly high gas mass fraction in NGC 2782. As discussed in Sect. 3.1, the mass of the molecular gas in NGC 2782 is the most extreme of all the NUGA galaxies observed so far; within a region  $\sim 4$  kpc in diameter, the molecular gas comprises 7% of  $M_{\text{dyn}}$ . This centrally concentrated molecular gas could be the result of the interaction which NGC 2782 has undergone. A high gas mass fraction is a necessary condition for the decoupling of the secondary bar, and thus promotes infall. Finally, we could be observing NGC 2782 in a particularly favorable epoch for the fueling of its AGN. Future work on our statistical sample will help understand duty cycles and timescales for the creation and maintenance of active accretion in galactic nuclei.

## 8. Summary and conclusions

We summarize our main results as follows:

- (a) High-resolution  $^{12}\text{CO}$  observations of NGC 2782 obtained with the PdB interferometer show emission aligned with the stellar nuclear bar of radius  $\sim 1$  kpc. In  $^{12}\text{CO}(2-1)$ , we clearly resolve two spiral arms at high pitch angle along the nuclear bar; in the  $^{12}\text{CO}(1-0)$  maps, the gas changes direction to form the beginning of two straight dust lanes, aligned with an outer stellar oval reminiscent of a primary bar.
- (b) From the stellar gravitational potential inferred from the IRAC  $3.6 \mu\text{m}$  image and the gas density from the  $^{12}\text{CO}$  distributions, we compute the azimuthally-averaged torques exerted by the stellar bars on the gas. This calculation reveals systematically negative torques in NGC 2782, down to the resolution limit of our image.
- (c) The negative torques and the dynamics inferred from our observations are explained by a scenario which is consistent with existing radio, optical, and molecular-gas features in the circumnuclear region of the galaxy. Star formation occurs in an  $H\alpha$  ring-like structure encircling the nuclear bar at the ILR of the primary bar/oval. The gas traced by CO emission is infalling to the center as a result of gravity torques from the decoupled nuclear bar. The two high-pitch angle CO spiral arms are winding up toward the center in a nuclear ring, corresponding to the ILR of the nuclear bar.
- (d) This scenario is supported by N-body simulations which include gas dissipation, and reproduce the secondary bar decoupling, the formation of the elongated ring at the 1 kpc-radius ILR of the primary bar, and the gas inflow to the 200-300 pc-radius ILR of the nuclear bar.

The average negative torques revealed by our analysis show that infall to the central regions in NGC 2782 is occurring in the present epoch. Our numerical simulations suggest that the negative torques producing inflow are caused by the decoupling of the primary and nuclear bar. This is made possible by the high central mass concentration and large gas mass fraction in the galaxy, perhaps a result of the prior interaction which caused the stellar sheets, ripples, and HI tidal tails in its outer regions. Future work will help understand what conditions are necessary for fueling an AGN, and how the gas distribution, its kinematics, and the stellar gravitational potential interact to set the stage for gas inflow.

*Acknowledgements.* LKH sincerely thanks the LERMA-Observatoire de Paris for generous funding and kind hospitality during the writing of this paper. We would like to thank the anonymous referee for insightful questions which helped clarify the text. This research has made use of the NASA/IPAC Extragalactic Database (NED) which is operated by the Jet Propulsion Laboratory, California Institute of Technology, under contract with the National Aeronautics and Space Administration.

## References

- Allard, E. L., Knapen, J. H., Peletier, R. F., & Sarzi, M. 2006, *MNRAS*, 371, 1087
- Benedict, G. F., Howell, D. A., Jørgensen, I., Kenney, J. D. P., & Smith, B. J. 2002, *AJ*, 123, 1411
- Boone, F., Baker, A. J., Schinnerer, E., et al. 2007, *A&A*, 471, 113 (NUGA VII)
- Boer, B., Schulz, H., & Keel, W. C. 1992, *A&A*, 260, 67
- Bournaud, F., & Combes, F. 2002, *A&A*, 392, 83
- Bournaud, F., Combes, F., & Semelin, B. 2005, *MNRAS*, 364, L18
- Buta, R., & Block, D. L. 2001, *ApJ*, 550, 243
- Combes, F., García-Burillo, S., Boone, F., et al. 2004, *A&A*, 414, 857 (NUGA II)
- Combes, F., Debbasch, F., Friedli, D., & Pfenniger, D. 1990, *A&A*, 233, 82
- Combes, F., & Gerin, M. 1985, *A&A*, 150, 327
- Combes, F., & Sanders, R. H. 1981, *A&A*, 96, 164
- de Jong, R. S. 1996, *A&A*, 313, 377
- Devereux, N. A. 1989, *ApJ*, 346, 126
- Englmaier, P., & Shlosman, I. 2004, *ApJ*, 617, L115
- Ferrarese, L., Pogge, R. W., Peterson, B. M., Merritt, D., Wandel, A., & Joseph, C. L. 2001, *ApJ*, 555, L79
- Freeman, K. C. 1992, *Physics of Nearby Galaxies: Nature or Nurture?*, 201
- Friedli, D., & Martinet, L. 1993, *A&A*, 277, 27
- García-Burillo, S., Combes, F., Hunt, L. K., et al. 2003, *A&A*, 407, 485 (NUGA I)
- García-Burillo, S., Combes, F., Schinnerer, E., Boone, F., & Hunt, L. K. 2005, *A&A*, 441, 1011 (NUGA IV)
- García-Burillo, S., Combes, F., Usero, A., & Graciá-Carpio, J. 2007, *New Astronomy Review*, 51, 160
- Heller, C., Shlosman, I., & Englmaier, P. 2001, *ApJ*, 553, 661
- Janiuk, A., Czerny, B., Siemiginowska, A., & Szczerba, R. 2004, *ApJ*, 602, 595
- Heckman, T. M., Kauffmann, G., Brinchmann, J., Charlot, S., Tremonti, C., & White, S. D. M. 2004, *ApJ*, 613, 109
- Holtzman, J. A., Burrows, C. J., Casertano, S., Hester, J. J., Trauger, J. T., Watson, A. M., & Worthey, G. 1995, *PASP*, 107, 1065
- Hopkins, P. F., & Hernquist, L. 2006, *ApJS*, 166, 1
- Hunt, L. K., & Giovanardi, C. 1992, *AJ*, 104, 1018
- Hunt, L. K., & Malkan, M. A. 1999, *ApJ*, 516, 660
- Hunt, L. K., Pierini, D., & Giovanardi, C. 2004, *A&A*, 414, 905
- Ishizuki, S. 1994, in *IAU Colloq. 140, Astronomy with Millimeter and Submillimeter Wave Interferometry*, ed. M. Ishiguro & J. M. Welch (ASP Conf. Ser. 59; San Francisco: ASP), 292
- Jogee, S., Kenney, J. D. P., & Smith, B. J. 1998, *ApJ*, 494, L185
- Jogee, S., Kenney, J. D. P., & Smith, B. J. 1999, *ApJ*, 526, 665
- Jogee, S., Scoville, N., & Kenney, J. D. P. 2005, *ApJ*, 630, 837
- Kent, S. M. 1987, *AJ*, 93, 816
- King, A. R., & Pringle, J. E. 2007, *MNRAS*, in press (*astro-ph/0701679*)
- Knapen, J. H., Pérez-Ramírez, D., & Laine, S. 2002, *MNRAS*, 337, 808
- Krips, M., Eckart, A., Neri, R., et al. 2005, *A&A*, 442, 479 (NUGA III)
- Krips, M., Eckart, A., Krichbaum, T. P., et al. 2007, *A&A*, 464, 553 (NUGA V)
- Laurikainen, E., & Salo, H. 2002, *MNRAS*, 337, 1118
- Lequeux, J. 1983, *A&A*, 125, 394
- Makovoz, D., & Marleau, F. R. 2005, *PASP*, 117, 1113
- Maoz, D., Barth, A. J., Sternberg, A., et al., *AJ*, 111, 2248
- Marecki, A., Spencer, R. E., & Kunert, M. 2003, *Publications of the Astronomical Society of Australia*, 20, 46
- Moriondo, G., Giovanardi, C., & Hunt, L. K. 1998, *A&AS*, 130, 81
- Mould, J. R., Huchra, John P., Freedman, Wendy L., et al. 2000, *ApJ*, 529, 786
- Mulchaey, J. S., & Regan, M. W. 1997, *ApJ*, 482, L135
- Narayanan, D., Cox, T. J., Robertson, B., et al. 2006, *ApJ*, 642, L107
- Peng, C. Y., Ho, L. C., Impey, C. D., & Rix, H.-W. 2002, *AJ*, 124, 266
- Persic, M., Salucci, P., & Stel, F. 1996, *MNRAS*, 281, 27
- Pfenniger, D., & Friedli, D. 1993, *A&A*, 270, 561
- Quillen, A. C., Frogel, J. A., & Gonzalez, R. A. 1994, *ApJ*, 437, 162
- Saikia, D. J., Pedlar, A., Unger, S. W., & Axon, D. J. 1994, *MNRAS*, 270, 46
- Sakamoto, K., Okumura, S. K., Ishizuki, S., & Scoville, N. Z. 1999, *ApJ*, 525, 691
- Schweizer, F., & Seitzer, P. 1988, *ApJ*, 328, 88
- Smith, B. J. 1991, *ApJ*, 378, 39
- Smith, B. J. 1994, *AJ*, 107, 1695
- Smith, B. J., Struck, C., Kenney, J. D. P., & Jogee, S. 1999, *AJ*, 117, 1237
- Solomon, P. M., & Barrett, J. W. 1991, *Dynamics of Galaxies and Their Molecular Cloud Distributions*, 146, 235
- Yoshida, M., Taniguchi, Y., & Murayama, T. 1999, *AJ*, 117, 1158
- Young, J. S., Xie, S., Tacconi, L., et al. 1995, *ApJS*, 98, 219
- Zhang, J. S., Henkel, C., Kadler, M., et al. 2006, *A&A*, 450, 933

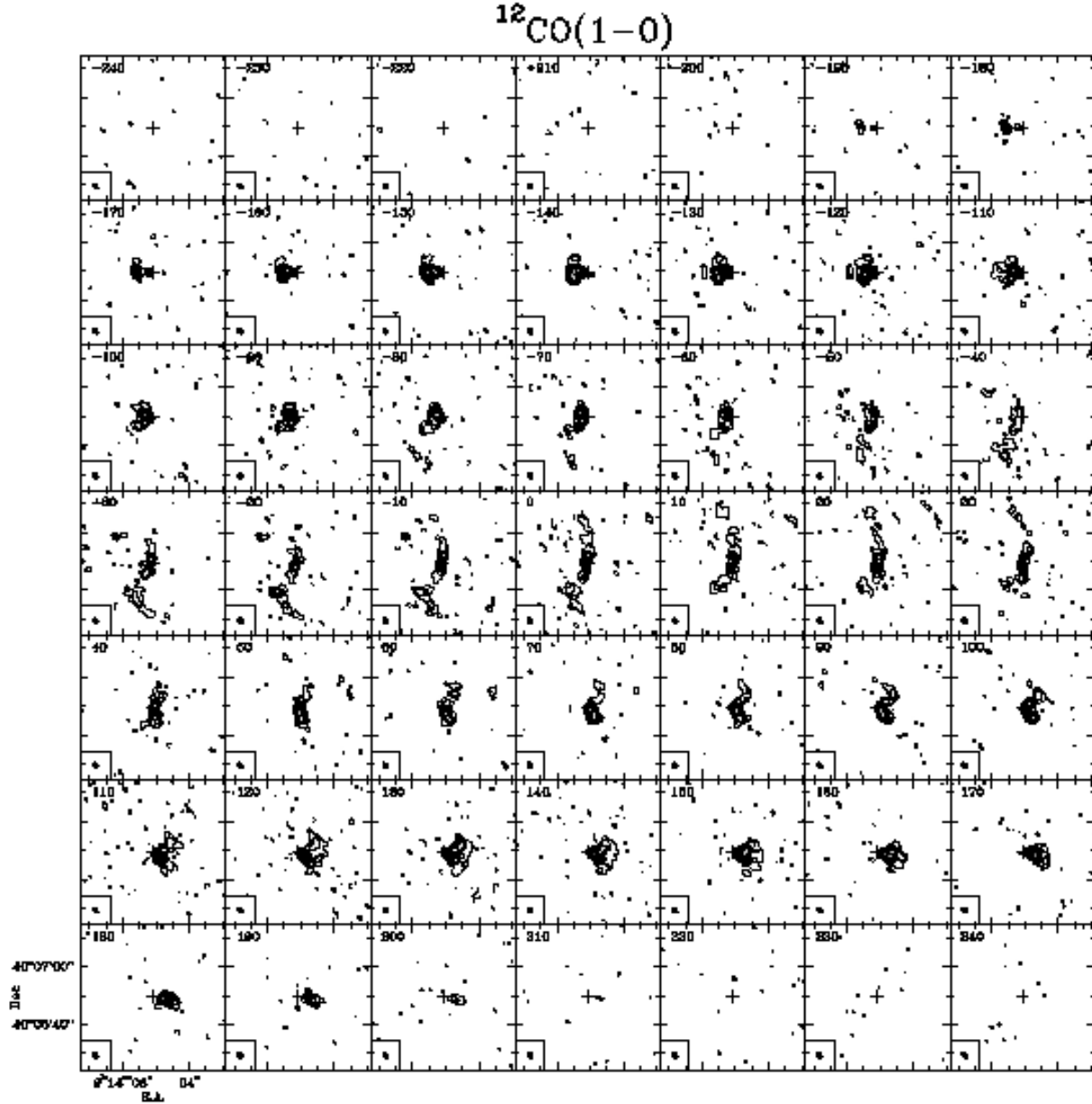


**Fig. 1.**  $^{12}\text{CO}(1-0)$  velocity-channel maps observed with the PdBI in the nucleus of NGC 2782 with a spatial resolution of  $2.1'' \times 1.5''$  at  $\text{PA}=38^\circ$  (beam is plotted as a filled ellipse in the bottom left corner of each panel). We show a field of view of  $50''$ , i.e.  $\sim 1.2$  times the diameter of the primary beam at 115 GHz. The phase tracking center is indicated by a cross at  $\alpha_{J2000}=09^{\text{h}}14^{\text{m}}05.08^{\text{s}}$  and  $\delta_{J2000}=40^\circ06'49.4''$ . Velocity-channels are displayed from  $v=-240 \text{ km s}^{-1}$  to  $v=240 \text{ km s}^{-1}$  in steps of  $10 \text{ km s}^{-1}$ . Velocities are in LSR scale and refer to  $v=2562 \text{ km s}^{-1}$ . Contour levels are  $-3\sigma$ ,

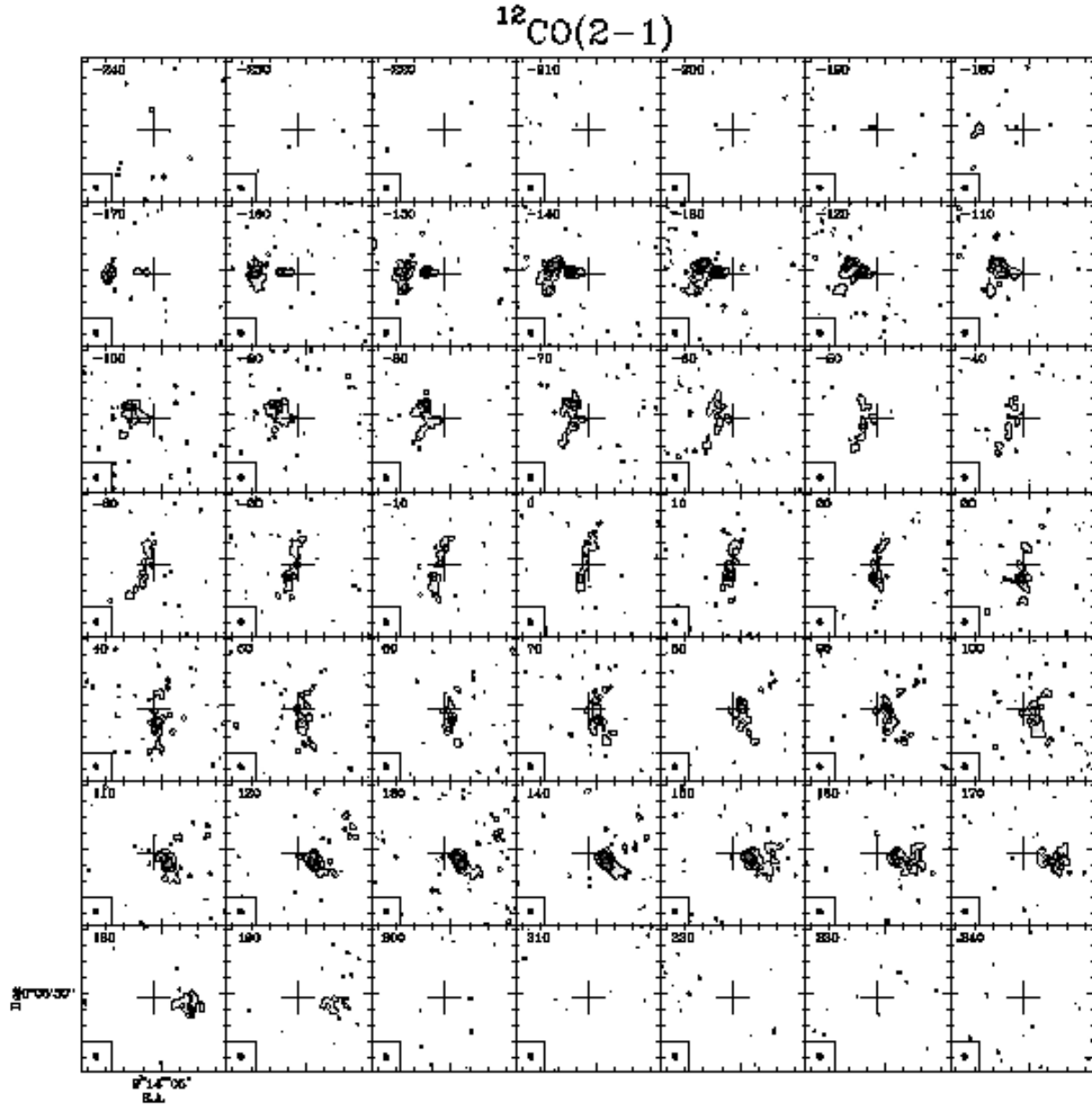


**Fig. 2.** Same as Fig. 1 but for the 2–1 line of  $^{12}\text{CO}$ . Spatial resolution reaches  $0.7'' \times 0.6''$  at  $\text{PA}=20^\circ$  (beam is plotted as a filled ellipse in the bottom left corner of each panel). We show a field of view of  $18''$ , i.e.  $\sim 0.9$  times the diameter of the the primary beam at 230 GHz. Velocity-channels are displayed from  $v=-240 \text{ km s}^{-1}$  to  $v=240 \text{ km s}^{-1}$  in steps of  $10 \text{ km s}^{-1}$ , with same reference as used in Fig. 1. Contour levels are  $-3\sigma$ ,  $3\sigma$ ,  $7\sigma$ ,  $10\sigma$ ,  $14\sigma$  and  $18\sigma$ , where the rms  $\sigma=5.2 \text{ mJy beam}^{-1}$ .

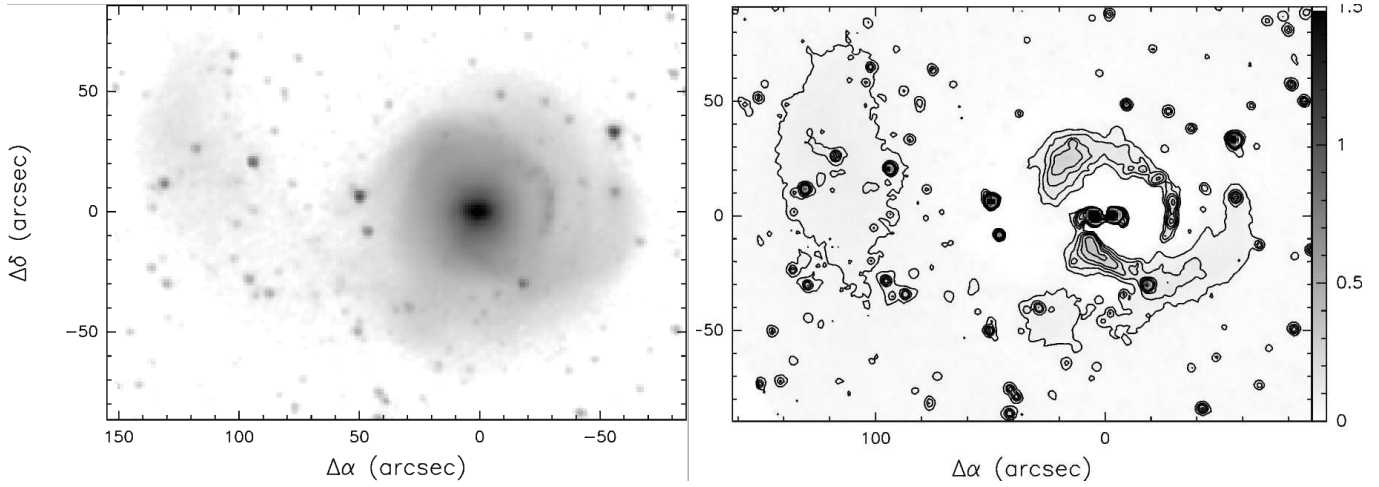


**Fig. 8.** Left panel: **a)** IRAC  $3.6 \mu\text{m}$  image of NGC 2782. The stellar sheets to the east and west, and the ripples about  $\sim 40''$  to the east are clearly visible. Right panel: **b)** IRAC  $3.6 \mu\text{m}$  residuals from the bulge-to-disk decomposition described in Sect. 4.1, with contours superimposed.

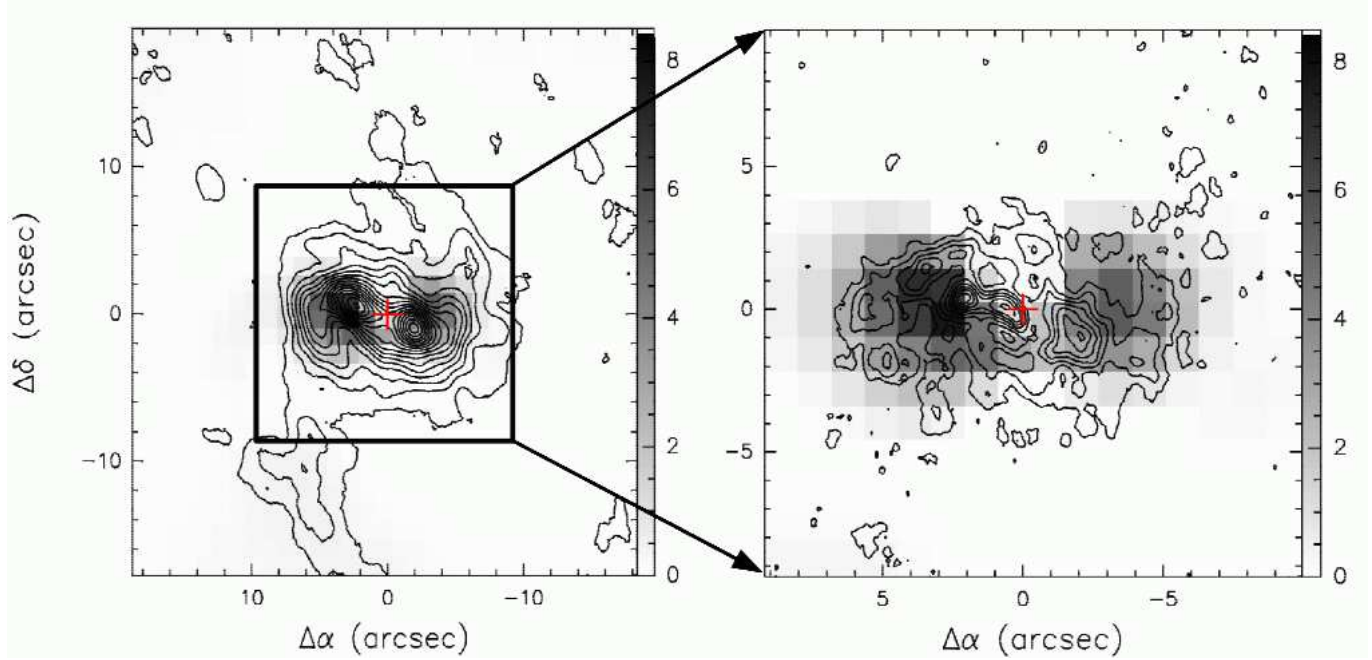


**Fig. 9.** Left panel: **a)** shows CO(1-0) total intensity contours overlaid on the gray-scale *residuals* (in MJy/sr) of the bulge-disk decomposition performed on the  $3.6 \mu\text{m}$  IRAC image. Right panel: **b)** shows the analogous overlay of CO(2-1). The phase-tracking center is shown by a cross.

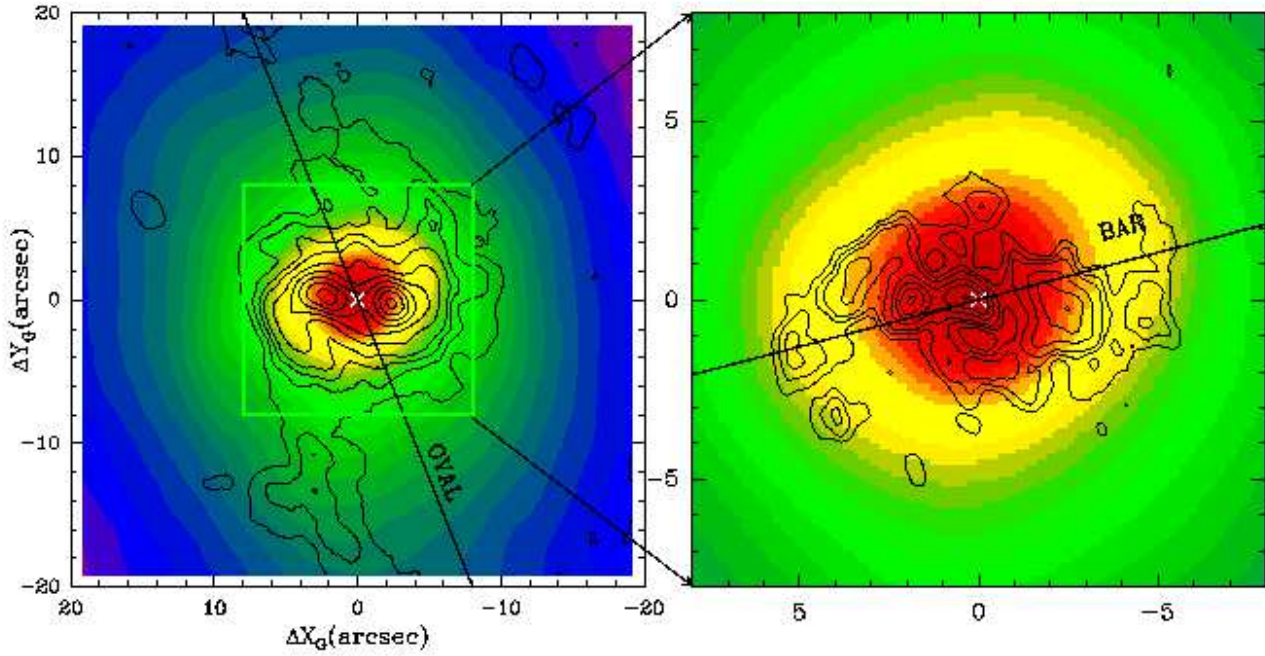


**Fig. 12.** Left panel: **a)**  $^{12}\text{CO}(1-0)$  total intensity contoured over a false-color representation the IRAC  $3.6\ \mu\text{m}$  image. Unlike Fig. 7, both the IRAC and the CO images have been deprojected onto the galaxy plane and rotated (by  $15^\circ$ ) so that the major axis is horizontal; units on  $(x, y)$  axes ( $\Delta X_G/\Delta Y_G$ ) correspond to arcsec offsets along the major/minor axes with respect to the AGN. The outer oval and stellar bar are marked by solid lines (in the deprojected rotated coordinate system). The image field-of-view is  $\sim 2.2\text{ kpc}$  in diameter. The  $\phi_i$ -angles are measured from the  $+X$  axis in the counter-clockwise direction. Right panel: **b)** The same for  $^{12}\text{CO}(2-1)$ .

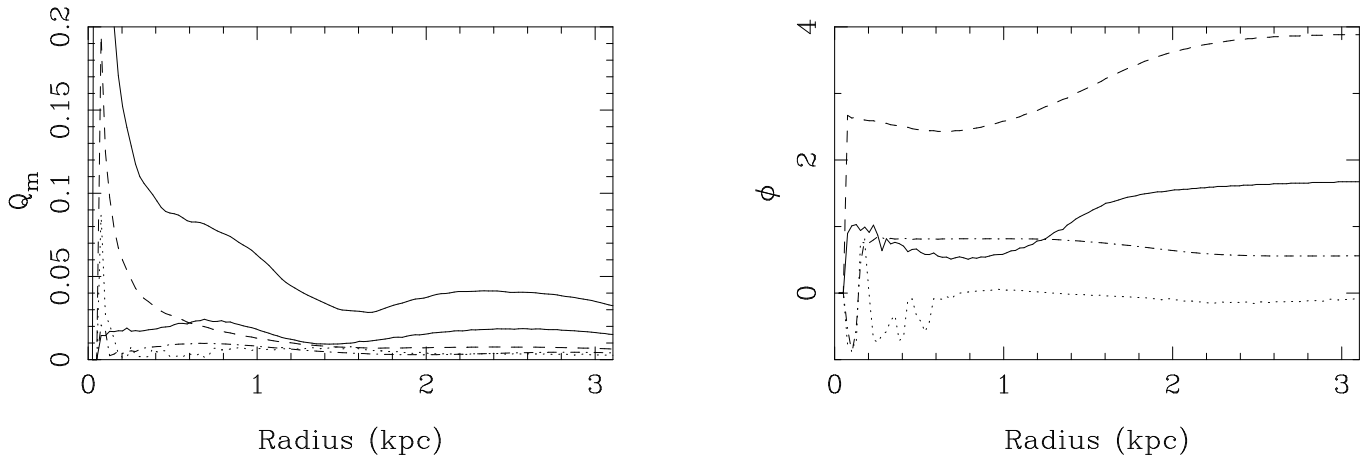


**Fig. 13.** Left panel: **a)** The different normalised Fourier components  $Q_m$  (defined in Eq. 3, as the maximum tangential force, normalised to the radial force), for the potential of NGC 2782, derived from the NIR image. The top solid line is the total tangential force  $Q_t$ , the next solid line is  $Q_2$ , the dashed line  $Q_1$ , the dotted line  $Q_3$ , and the dotted-dashed one  $Q_4$ . Right panel: **b)** The corresponding phases  $\theta_m$  in radians, defined in Eq. 1, with the lines as in the left panel.



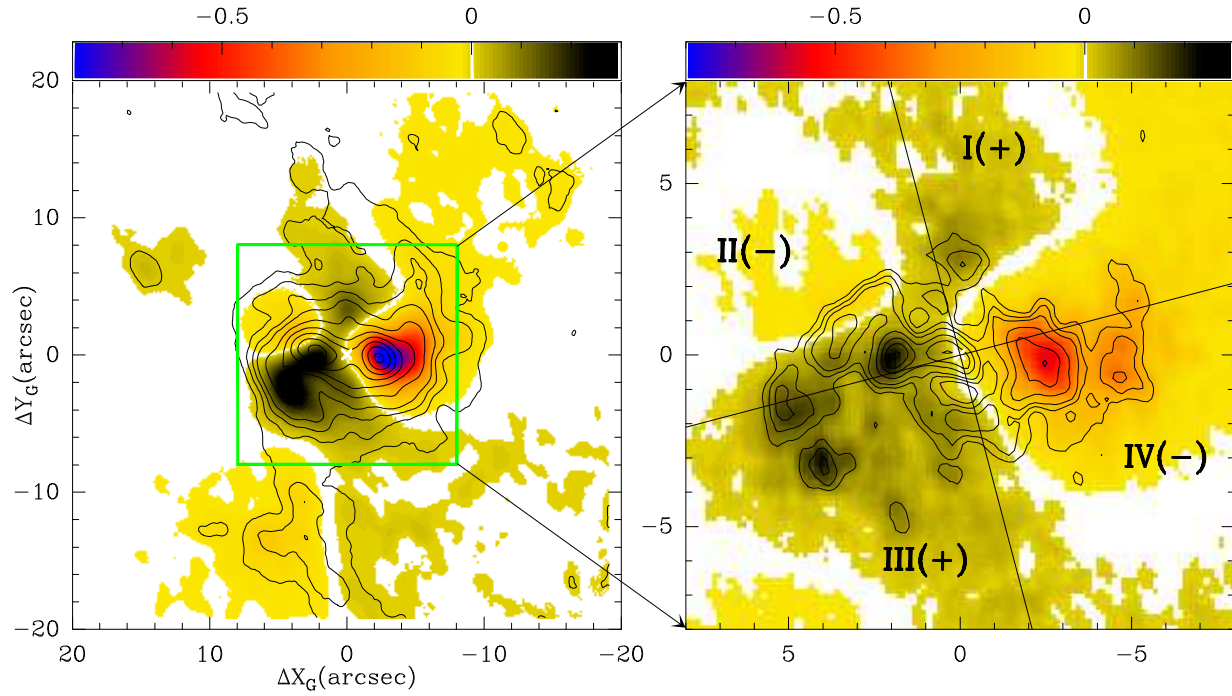


**Fig. 14.** Left panel: **a)**  $^{12}\text{CO}(1-0)$  total intensity contoured over a false-color representation of the torque maps  $\tau$  derived as described in the text. As in Fig. 12, this is the deprojected representation, with units on  $(x, y)$  axes ( $\Delta X_G/\Delta Y_G$ ) corresponding to arcsec offsets along the major/minor axes with respect to the AGN. The torque exerted on the spiral arm to the south is clearly associated with the outer oval. Right panel: **b)** The same for  $^{12}\text{CO}(2-1)$ . Both panels show the typical butterfly diagram due to an  $m = 2$  perturbation, and in **b)** we have marked the four quadrants with their positive (I, III) and negative torques (II, IV) which drive the gas outward and inward, respectively. As described in the text, the sign of the torques is determined by the rotation direction of the gas, namely clockwise in NGC 2782.

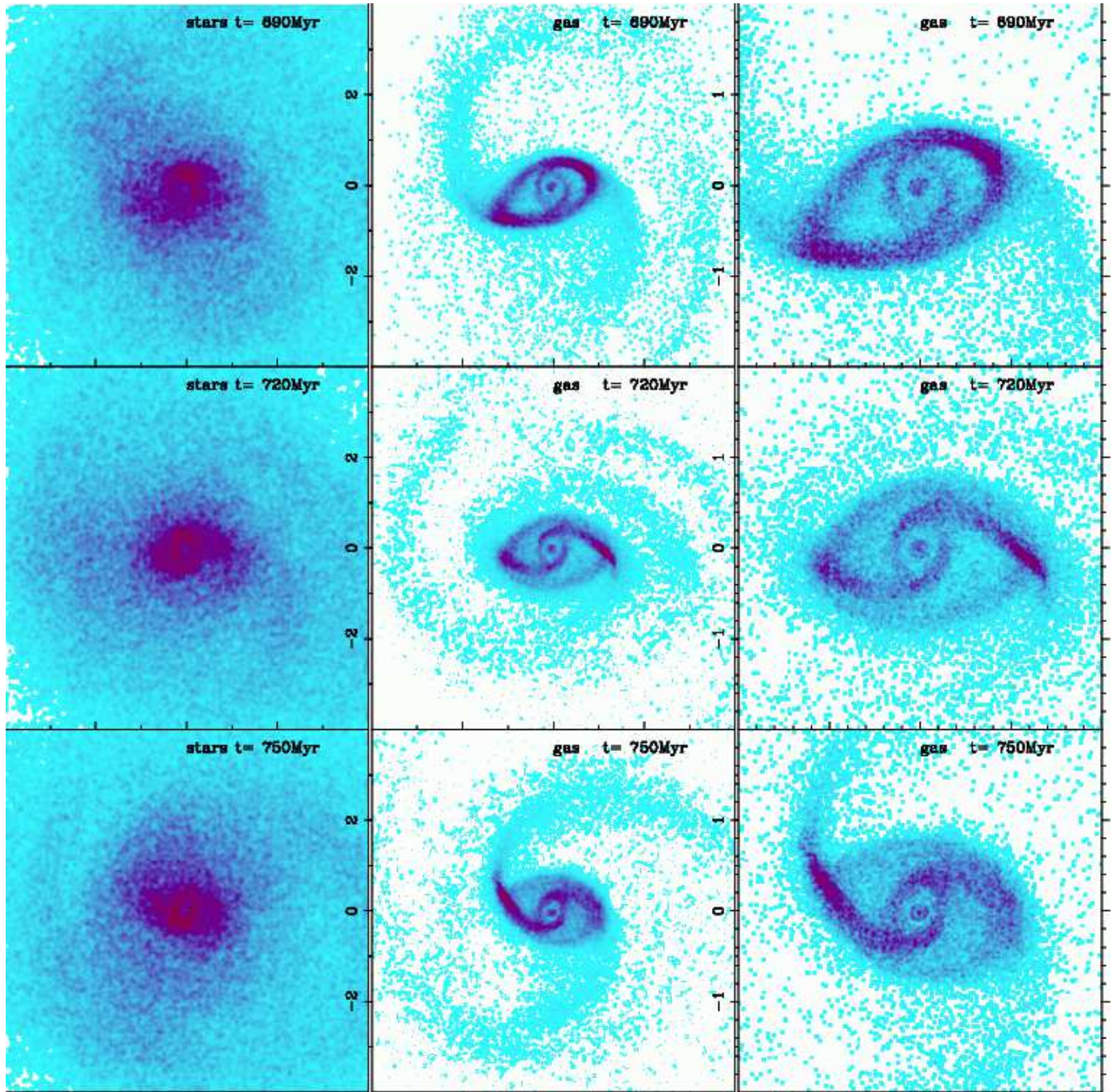


**Fig. 17.** **Left panel:** False-color plot of the stellar component distribution, in Run A (the intensity scale is linear and axes are in kpc). **Middle:** False-color plot of the corresponding gaseous component (the intensity scale is logarithmic). **Right:** Same as the middle panel, but with an expanded spatial scale. It can be seen that the gas which was predominantly in the more external ring (ILR of the primary bar) at  $T = 690$  Myr, is falling progressively inward, and is primarily inside the ILR at  $T = 750$  Myr. The gas infalling along the “dust lanes” is aligned along the nuclear bar, where the CO is observed in NGC 2782.

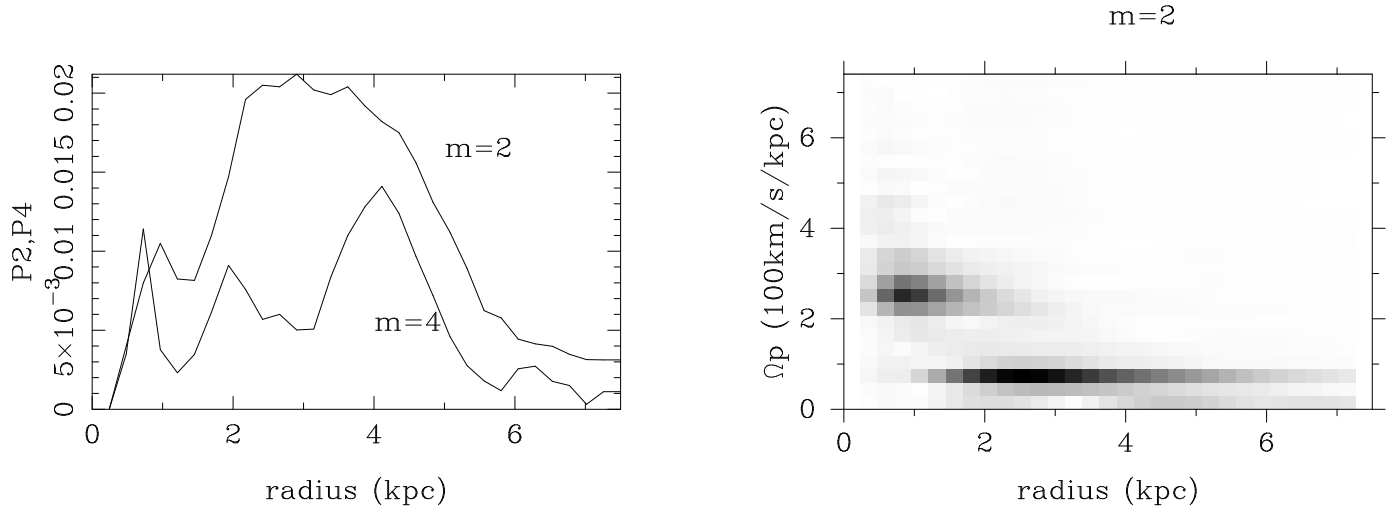


**Fig. 18.** **Left:** Intensity of the  $m = 2$  and  $m = 4$  Fourier components of the potential in Run A, during the second bar decoupling. **Right:** Power spectrum of the  $m = 2$  Fourier component, giving the pattern speed as a function of radius, during a period of 100Myr corresponding to the coexistence of the two bars. Since the pattern speed of the nuclear bar varies with time during this period, its  $\Omega_b$  signature is somewhat widened.